Robust theoretical modelling of core ionisation edges for quantitative electron energy loss spectroscopy of B- and N-doped graphene

T. P. Hardcastle[1,2], C. R. Seabourne[2], D. M. Kepaptsoglou[1], T. Susi[3], R. J. Nicholls[4], R. M. D. Brydson[1,2], A.J. Scott[2] and Q. M. Ramasse[1]

[1]*SuperSTEM Laboratory, STFC Daresbury Campus, Daresbury, WA4 4AD, UK*

[2]*School of Chemical and Process Engineering, University of Leeds, Leeds LS2 9JT, UK*

[3]*Faculty of Physics, University of Vienna, Boltzmanngasse 5, 1090 Vienna, Austria*

[4]*Department of Materials, University of Oxford, Oxford, OX1 3PH, UK*

Abstract

Electron energy loss spectroscopy (EELS) is a powerful tool for understanding the chemical structure of materials down to the atomic level, but challenges remain in accurately and quantitatively modelling the response. We compare comprehensive theoretical density functional theory (DFT) calculations of 1s core-level EEL *K*-edge spectra of pure, B-doped and N-doped graphene with and without a core-hole to previously published atomic-resolution experimental electron microscopy data. The ground state approximation is found in this specific system to perform consistently better than the core-hole approximation. The impact of including or excluding a core-hole on the resultant theoretical band structures, densities of states, electron densities and EEL spectra were all thoroughly examined and compared. These results are interpreted as an indicator of the overriding need for theorists to embrace many-body effects in the pursuit of accuracy in theoretical spectroscopy instead of a system-tailored approach whose approximations are selected empirically.

I. INTRODUCTION

A. Background

Graphene[1] has inspired new thinking in the emerging field of nanoelectronics[2] to move beyond the silicon-based technology of the last seventy years. Operating frequencies of early graphene-based field-effect transistor (GFET) prototypes[3-5] have quickly progressed to hundreds of GHz,[6,7] and basic issues such as graphene's absent band gap have inspired alternative approaches such as graphene nanoribbons,[8,9] bilayers,[10,11] strained graphene[12-14] and even the adoption of non-Boolean logic.[15] Significant milestones have been reached, for instance through to the use of hexagonal boron nitride as a supporting substrate[16] or *via* a novel nanowire-based GFET top-gate

improving device quality,[17] and some studies have already demonstrated fully-operational graphene-based integrated circuits for radiofrequency applications.[18,19] More recently, alternative 2D materials including MoS_2[20] and black phosphorous[21-23] have received some considerable attention. In any case, it is generally agreed that the ability to manipulate the electronic structure of graphene is a highly desirable and powerful tool for nanoscale device optimisation. This is not only because of the many possible physical and chemical functions graphene may perform in emerging consumer and industrial products, but also in a wider context because achieving precise control at the nanoscale is one of the primary motivations of the nanotechnology paradigm. Doping a material with a view to create an excess of electrons or holes is one such technique for tailoring its electronic structure, and the obvious candidates dopant elements for graphene are B (p-type) and N (n-type) due to their locations in the periodic table. Nitrogen-doped graphene (N-graphene) has been extensively studied in the context of catalysts,[24-27] batteries,[28] supercapacitors[29,30] and biosensors,[31] as has B-graphene for fuel cells,[32] solar cells,[33] supercapacitors,[34] and spin-filtering nanoribbons.[35]

The electronic structure of 2D materials can be probed directly in the microscope at the single atom level using electron energy loss spectroscopy (EELS) which is a particularly revealing tool when combined with theoretical electronic structure calculations. In 2013, Bangert *et al*.[36] used low-energy ion implantation to dope single layer graphene with B and N and it was found that for sufficiently low implantation energies the vast majority of dopants were substitutionally incorporated into the graphene lattice. Our group subsequently obtained atomically-resolved electron energy loss (EEL) *K*-edge spectra of the substitutional N and B dopants in graphene using aberration-corrected scanning transmission electron microscopy (STEM)[37] and by comparison with well-matched ground state (*i.e*. without considering a 1*s* core-hole induced by the incoming electron beam) density functional theory (DFT)[38,39] calculations, it was argued that the EEL spectra provided direct experimental evidence of the expected p- and n-type doping in the samples. The substitutional N-graphene defect has been studied before by Nicholls *et al*.[40], and its *K* edge spectrum by Warner *et al*.[41], and Arenal *et al*.[42], and also by Lin *et al*.[43] for the N-graphite case, but the B-graphene *K*-edge spectrum was shown for the first time in the aforementioned study[37] to possess an unusual and broad profile for an sp^2-bonded material, and was checked by repeated accumulation of the spectrum within a small subscan window using the procedure described in Ramasse *et al*.[44] The motivation of the present work is to extend the analysis of our previous study[37] to include core-hole calculations and to evaluate their validity in the specific case of N- and B- doped graphene. Our evidence indicates that the ground state approximation is quite successful at matching

experimental data, whereas calculations making use of the core-hole approximation either fail to significantly improve this match, or severely worsen it.

B. Core-level spectroscopy of 2D materials with pseudopotentials

In the general case, the relative probability of a scattering electron losing an amount of energy within the range E and $E + dE$ and scattering into the infinitesimal solid angle $d\Omega$ is given by the differential cross section[45],

$$\frac{d^2\sigma}{d\Omega dE} = \frac{1}{(\pi e a_0)^2}\frac{1}{|\vec{q}|} Im\left(\frac{-1}{\varepsilon(\vec{q},\omega)}\right) = \frac{1}{(\pi e a_0)^2}\frac{1}{|\vec{q}|}\left(\frac{\varepsilon_2(\vec{q},\omega)}{\varepsilon_1^2(\vec{q},\omega)+\varepsilon_2^2(\vec{q},\omega)}\right), \quad (1)$$

where $a_0 = 0.529 \times 10^{-10}$m (3.s.f.) is the first Bohr radius, e is the electron charge, $\vec{q}$ is the scattering vector, $\varepsilon = \varepsilon_1 + i\varepsilon_2$ is the dielectric function (sometimes called the loss function) and $\omega = E/\hbar$. An EEL spectrum is a direct measurement of the scattering cross section, so EELS peaks occur at energies E and scattering vectors $\vec{q}$ where the functions ε_1 and ε_2 approach values causing the expression $\varepsilon_2/(\varepsilon_1^2 + \varepsilon_2^2)$ to peak. The polarizability of the system, characterised by collective electron motion, is given by the quantity $Re(\varepsilon - 1) = \varepsilon_1 - 1$, whereas the imaginary component ε_2 gives the absorption properties, characterised by single-particle transitions between eigenstates. For low energy excitations characterised by plasmons, interband transitions and intraband transitions with E of the order ~10 eV, it is necessary to calculate both ε_1 and ε_2 to calculate the EELS which accounts for both polarization and absorption effects. In this low energy regime it is desirable to account for the dynamic response of the system to an external perturbation, involving a description of the induced change in the electron density. Calculating such a spectrum theoretically can be achieved using time-dependent[46] (TD) DFT and consists of calculating the response function[47] $\chi = \varepsilon - 1$ by self-consistently solving a Dyson equation $\chi = \chi_0 + \chi_0 K \chi$ (to first order in perturbation theory) where χ_0 is the non-interacting response function found directly from the Kohn Sham eigenstates using the formula of Adler and Wiser, [48] [49] and K is the time-dependent exchange correlation kernel. Nazarov[50] has pointed out that for 2D materials modelled under periodic boundary conditions (which are strictly exotic 3D systems with effective 2D properties by virtue of the vacuum gap) this approach has difficulties because of the slowly-decaying electric field between the material and its periodic images separated by distance d which decays as ~$e^{-|\vec{q}|d}$,[1] and suggested that this problem can be solved by using a modified loss function in a TDDFT framework to calculate EELS which excludes out-of-plane $\vec{q}$ vectors from equation (1) by design. A more recent paper[51] by Nazarov provides details of a formalism whereby the quantum mechanical motion of the incoming fast electron is treated explicitly as a complex charge density

[1] Here, e is the mathematical constant, not the electronic charge.

defined using solutions to the Lippmann-Schwinger equation. Such developments in theoretical modelling are timely for 2D materials because the physical nature of low energy excitations in graphene has caused some controversy in the literature[52-56] which is symptomatic of the failure of theoretical models to properly rationalise experimental observations. In the case of high energy excitations where E is of the order of a few hundred eV, $\varepsilon_1 = 1$ corresponding to zero polarizability, and ε_2 becomes small. At these high energies, the perturbation is far higher than the energies associated with the collective electron resonances, and so only absorptions, determined by ε_2, are measured. In this limit, $\varepsilon_2/(\varepsilon_1^2 + \varepsilon_2^2) \rightarrow \varepsilon_2$ and so the spectrum is directly proportional to ε_2. This simplifies the situation significantly because the EEL spectrum only depends on transitions between eigenstates and can be calculated with full validity by just considering these transitions. In this scenario, the critical requirement in the case of 2D materials modelled under 3D periodic boundary conditions is that the spectrum be converged with respect to the vacuum distance, corresponding to zero overlap between the ground state wavefunctions along the vacuum direction. This work uses calculations of this sort, and details of such convergence tests for the supercells considered in this work are given in the Supplementary Information. The interactions between the system's electrons and the beam-induced core hole can, however, still play a significant role. A two-particle description such as the Bethe Salpeter equation[57] (BSE) is usually necessary to properly describe electron-hole interactions, although the computational demands of this approach are prohibitively high for the supercells used in this study. In a general periodic framework in the high-energy regime, the core-level EEL spectrum is given by Ehrenreich and Cohen's formula,[58]

$$\varepsilon_2(\vec{q}, E) = \frac{4\pi e^2}{|\vec{q}|^2 \Omega} \sum_{m}^{unocc.} \left|\langle \psi_c | e^{i\vec{q}.\vec{r}} | \psi_m \rangle\right|^2 \delta\big(E - (E_m - E_c)\big), \quad (2)$$

where Ω is the volume of the periodic cell, $|\psi_c\rangle$ is the core state, $|\psi_m\rangle$ are the unoccupied states, $e^{i\vec{q}.\vec{r}}$ is the matrix perturbation term representing the scattering event with scattering wavevector $\vec{q}$ and excited electron position $\vec{r}$, E_m and E_c give the energies of the unoccupied and core states respectively, and the delta function gives the density of states (DOS) of the final states $|\psi_m\rangle$. The perturbation $e^{i\vec{q}.\vec{r}}$ can be accurately treated at the level of the dipole approximation for which $|\vec{q}| \rightarrow 0$ if the collection aperture semi-angle is small compared to the maximum scattering vector considered in the experiment.[59] The consequence of the dipole approximation is that only transitions for which the angular momentum quantum number l changes by ±1 are attributable to the spectrum, so the DOS with $l = 1$, *i.e.* the p DOS, is of primary interest because it reveals EELS-active states. In plane-wave DFT, Kohn-Sham states implicitly satisfy the requirement of electron indistinguishability and so no state can be rigorously associated with any of the atomic nuclei. Projection of the converged density onto locally

well-defined linear combination of atomic orbitals (LCAO) *p* states[60] is therefore needed to recover local information and allow a meaningful discussion of states which are attributable to the spectrum of the dopant nucleus. This is achieved in this work by using the projection technique of Sanchez-Portal[61] as implemented in CASTEP by Segall *et al*.[62] In the $|\vec{q}| \to 0$ limit, $e^{i\vec{q}.\vec{r}} \approx 1 + \vec{q}.\vec{r}$ and the term $\vec{q}.\vec{r}$ can be written as the dipole operator $|\vec{q}|\hat{u}.\vec{r}$ where $\hat{u}$ is a unit vector. The term $\langle\psi_c|1|\psi_m\rangle$ is clearly zero because $|\psi_c\rangle$ and $|\psi_m\rangle$ are orthogonal and the $|\vec{q}|$ term in the matrix element $\langle\psi_c||\vec{q}|\hat{u}.\vec{r}|\psi_m\rangle$ clearly cancels with $|\vec{q}|^2$ on the denominator before the summation in equation (2) so that the matrix elements are given by $\langle\psi_c|\hat{u}.\vec{r}|\psi_m\rangle$. Thus, using periodic boundary conditions and a finite grid of *k* points to sample the Brillouin zone, the EEL spectrum under the dipole approximation can be found with ground state DFT eigenstates as follows:

$$EELS(E) = \varepsilon_2(|\vec{q}| \to 0\,, E) = \frac{4\pi e^2}{\Omega} \sum_{m}^{unocc.} \sum_{\vec{k}}^{BZ} \left|\langle\psi_c|\hat{u}.\vec{r}|\psi_{m,\vec{k}}\rangle\right|^2 \delta\left(E - \left(E_{m,\vec{k}} - E_c\right)\right) \quad (3)$$

where the sum over m includes all unoccupied bands in the calculation, the sum over $\vec{k}$ includes all *k* points in the Brillouin zone, $\psi_{m,\vec{k}}$ is the all-electron Kohn Sham wavefunction evaluated in the m^{th} band at k point $\vec{k}$, and $E_{m,\vec{k}}$ is the energy eigenvalue of the state $\psi_{m,\vec{k}}$. Since the core-level spectra are found by evaluating the perturbation matrix elements between a core state and an all-electron unoccupied state, it is perhaps not initially obvious how this is achieved in a pseudopotential setting. In fact, this can be achieved using Blöchl's[63] projector-augmented wave (PAW) formalism developed and implemented[64] for pseudopotentials in CASTEP,[65] in which the all-electron eigenstates $\psi_{m,\vec{k}}$ can be reconstructed by performing a linear transformation on the pseudoeigenstates $\tilde{\psi}_{m,\vec{k}}$ found in the supercell calculation. The matrix elements in the EELS formula (3) are therefore reconstructed using the relation given by the projector augmented wave (PAW) method:

$$\langle\psi_c|\hat{u}.\vec{r}|\psi_{m,\vec{k}}\rangle = \langle\psi_c|\hat{u}.\vec{r}|\tilde{\psi}_{m,\vec{k}}\rangle + \sum_i \left(\langle\psi_c|\hat{u}.\vec{r}|\phi_i\rangle + \langle\psi_c|\hat{u}.\vec{r}|\tilde{\phi}_i\rangle\right)\langle\tilde{p}_i|\tilde{\psi}_{m,\vec{k}}\rangle$$

where ϕ_i are the all-electron partial waves, $\tilde{\phi}_i$ are the pseudo-partial waves and $\tilde{p}_i$ are the projector functions, orthogonal to the pseudopartial waves $\tilde{\phi}_i$ by design. The core state comes from a separate all-electron calculation on a single isolated atom. This approach retains the efficiency of pseudopotentials and plane waves while allowing a meaningful calculation of core-to-conduction-band transition probabilities. A full-electron core-hole can be included implicitly by using Pickard's method[66] to self-consistently derive an excited pseudopotential from an all-electron calculation of a single atom from which the core state is explicitly removed. It is very important to note that when using an excited pseudopotential to represent the core-hole, the fully minimised electronic structure that results is also a *ground state* system. The "excited" pseudopotential

modifies the local environment such that the Kohn-Sham (KS) equations, which are at the heart of DFT, can be solved self-consistently in the conventional way, where the core-hole is *frozen*. Thus, all calculations in this paper are strictly ground state calculations, where "core-hole" and "ground state", used subsequently, refer to calculations with and without excited pseudopotentials respectively. Full details of the PAW implementation for core-level spectroscopy in CASTEP are given by Gao *et al*.[64]

II. METHOD

A. Convergence parameters

All calculations were carried out using the plane-wave DFT code CASTEP with self-consistently-generated on-the-fly pseudopotentials. Local total-energy functionals, which depend only on the density $n(\vec{r})$, and semi-local functionals, which depend on both $n(\vec{r})$ and spatial gradients $\nabla n(\vec{r})$, are much less computationally-demanding than non-local functionals (not considered) which include the density at multiple points $\vec{r}$ and $\vec{r}'$ as their arguments. The local density approximation (LDA)[39] is the simplest local functional, and validation tests performed in a previous study by our group[67] for graphite – a comparatively less-exotic bulk material than doped-graphene with uncontroversial experimentally-measured lattice parameters[68] – showed the generalized gradient approximation (GGA) PBE functional[69] combined with the Tkatchenko and Scheffler's van der Waals correction scheme[70] (PBE-TS) to be the most accurate semi-local functional. Thus, the LDA and PBE-TS functionals were selected and used to determine that k point spacings of less than 0.02 $Å^{-1}$ using a regular Monkhorst Pack[71] grid, a kinetic energy cutoff of 800 eV and a vacuum distance of 20 Å between layers were sufficient to converge the EEL spectra of periodic C_7N and C_7B graphene systems. These parameters were subsequently used throughout. The lattice parameter of pristine graphene using the hexagonal two-atom unit cell then optimised and found to be 2.464 Å (3 d. p.) for PBE+TS and 2.445 Å (3 d. p.) for LDA. Fully converged EEL spectra of single substitutional dopants were then calculated both with and without a core-hole in supercells relaxed using BFGS[72-76] optimisation of sizes 2×2, 4×4, 6×6, 7×7 and 8×8 with k points grids of 12×12×1, 6×6×1, 4×4×1, 4×4×1 and 3×3×1 respectively. All spectra were found to be satisfactorily converged for size 6×6 and above (see Supplementary Information), and 7×7 graphene supercells of chemical formula $C_{97}B$, C_{98} and $C_{97}N$ were adopted for the main calculations.

B. Benchmarking - functional, charge neutralisation, relaxation timescales and the '3n rule'

Tests were then carried out on these relaxed structures with fully-converged parameters to assess *(i)* how much the spectra differ between the LDA and PBE-TS functionals *(ii)* how to neutralise the core-hole, *(iii)* how to best account for relaxation timescales in the material and *(iv)* some differences between 6×6 and 7×7 supercells relating to the '3*n* rule'[77] (explained briefly below). (i) The *K*-edge spectra were calculated using both the LDA and PBE-TS functionals, and both were found to be very similar in character and indicative of the same overall physical interpretation. Therefore only the PBE+TS calculations were used for the detailed physical analysis below while the LDA spectra are provided for completeness in the Supplementary Information. It was also shown recently that the LDA gives significantly worse core-level binding energies than GGAs.[78] (ii) A core-hole needs to be neutralised by either including a linear homogenous compensating background potential or including one additional Kohn-Sham state when optimising the then-core-excited state density. Once again, both methods were used for completeness and comparison. This approach is also easier to justify physically because it does not discriminate against any unoccupied state, whereas populating the lowest (half-) unoccupied band as in the latter approach has direct implications for the EEL spectrum immediately above the Fermi energy. (iii) Electron relaxation timescales are to the order of ~ 10^{-14} - 10^{-15} s,[79] whereas structural relaxation (i.e. of nuclear positions) is much slower at about ~ 10^{-11} - 10^{-12} s. For this reason, it is expected that structural relaxation in response to a beam-electron-induced core-hole has no influence on the energy loss of the transmitted electron, so all structures were relaxed without a core-hole. (iv) Although *K*-edge EEL spectra probe localised states, the issue of supercell size actually goes slightly beyond simply making the supercell large enough for a converged spectrum. This is because of the so-called '3*n* rule' for graphene with a single substitutional dopant, which states that the π and π* bands coincide, or nearly coincide, at the reciprocal supercell's gamma point ($\Gamma_{3n\times3n}$) rather than at the usual Dirac point ($K_{3n\times3n}$) if the supercell is formed from an array of 3*n*×3*n* unit cells, where *n* is any positive integer. As a consequence, while the density of a given Kohn-Sham state(s) may be clearly localised and smoothly convergent with increasing supercell size, that state can exhibit different band dispersion behaviour near the Fermi energy depending on the 3*n* rule. The issue is therefore only one of data interpretation – an issue worth mentioning, nevertheless – and illustrates the level of care needed when invoking the terminology typically associated with band theory (such as "π*" – see Results) for labelling spectral peaks. 7×7 supercells are used for the main *K* spectrum calculations, with the 6×6 cases summarised in the Supplementary Information for comparison.

C. Main calculations

The *K*-edge EEL spectra of substitutional N and B dopants in graphene were calculated using at least 2048 unoccupied bands in relaxed 7×7 supercells with and without a core-hole, and compared with experimental data. Lattice symmetries were fully exploited to reduce the computational load. Gaussian instrumental broadening was used with full-width-half-maxima (FWHM) of 0.3 eV, along with Lorentzian broadening to account for lifetime effects with FWHM of 0.16 eV, 0.17 eV and 0.18 eV for B, C and N respectively based on semi-empirical values.[80] The theoretical spectra were then rigidly shifted along the energy axis to achieve the best fit to the experimental data[37] and normalised to their highest peaks. Mizoguchi's edge-onset threshold energy cross-check for pseudopotentials[81] was also performed and it was confirmed that the edge onset energy calculated in this way approximately matches the experimental values. The optimised plane wave densities were projected onto LCAO *p* basis functions to obtain the *p* DOS associated with the nuclei of interest using OptaDOS[82] with the adaptive broadening scheme.[83] Band structures of the optimised electronic structures were evaluated along the high-symmetry paths $\Gamma_{7\times7} \rightarrow M_{7\times7} \rightarrow K_{7\times7} \rightarrow \Gamma_{7\times7}$ (where 7×7 in subscript signifies correspondence to the Brillouin zone of the entire 7×7 cell) by calculating the eigenvalues at a total of 11 distinct *k* points (distinct from the 4×4×1 Monkhorst Pack grid used for the EELS stage - see Supplementary Information) three of which were located exactly at $\Gamma_{7\times7}$, $M_{7\times7}$ and $K_{7\times7}$. All such k-spacings are smaller than 0.01 $Å^{-1}$. The EEL spectra, *p* DOS and band structures were all then aligned at their Fermi energies in order to allow a transparent analysis of the electronic structures underlying the calculated spectra.

D. Experimental details

The doped graphene specimens were prepared by low energy implantation free-standing graphene (prepared by chemical vapour deposition techniques). The implantation was performed directly on graphene suspended on Quantifoil Transmission Electron Microscopy grids. A detailed account of the synthesis conditions can be found in the previous works of Xu et al.[84] and Bangert et al.[36] Electron energy loss measurements from single N or B dopant atoms as well as and their single C neighbours in implanted graphene samples were performed on a Nion UltraSTEM100 aberration-corrected dedicated STEM instrument operated at 60 kV. A detailed description of the optical conditions and EELS acquisition parameters can be found in previous works by Bangert et al.[36] and Kepaptsoglou et al.[37]

III. RESULTS AND ANALYSIS

A. Initial checks

Figure 1 shows an experimental/theoretical comparison for the atomically-resolved (i)-(iii) boron, (iv)-(vi) carbon and (vii)-(ix) nitrogen *K* edge spectra, along with the corresponding band structures for each supercell. With the important exception of spectral features directly straddling the Fermi energy, a basic trend in the theoretical spectra is that a core-hole calculation results in a higher intensity of low energy features and a suppression of high energy features, compared to a ground state EELS calculation. This confirms a basic theoretical expectation: a core-hole causes both occupied and unoccupied states to sink to lower energies due to the increased attraction to the nucleus.

It is also worth briefly pointing out some trends in the band structures to verify the expected doping effects and to confirm the reasonableness and correctness of the calculations: The ground state C (*i.e.* pristine graphene) band structure in Fig. 1 (iv) exhibits a Dirac cone with the Fermi energy intersecting the Dirac point K_{7x7} as expected. Also, the band structures of the B (+core-hole) supercells in Figs. 1 (ii) and (iii) strongly resemble the pristine graphene band structure in Fig. 1 (iv). This follows basic intuition: the core-hole makes the B nucleus carbon-like, and the π^* band is either partially occupied (background potential) or fully occupied (extra Kohn-Sham state) depending on the core-hole neutralisation method, with the Fermi energy being shifted up to the Dirac point K_{7x7} in the latter case. There is an equivalent similarity between the ground state N supercell band structure in Fig. 1 (vii) and those of the two C (+core-hole) supercells in Fig. 1 (v) and (vi): in these cases, the core-hole makes the C nucleus nitrogen-like, and the Fermi level either fully populates the π band (background potential) or partially populates the π^* band (extra Kohn-Sham state). Small π/π^* band gaps are also observed at K_{7x7} with corresponding large gaps at Γ_{7x7} in Figures 1 (i) and 1 (vii) in agreement with Casolo's detailed symmetry arguments[85] for N and B dopants in the ground state. The same effect is observed for the C (+core-hole) supercells' bandstructures in Figures 1 (v) and 1 (vi) which also show the same small band gap at K_{7x7} where Casolo's arguments can be safely assumed to apply. Finally, we tested Zhou's '3n rule' by calculating band structures for 6x6 supercells (see Supplementary Information) and the π/π^* band gaps were found to be large at K_{6x6} and small at Γ_{6x6} as expected.

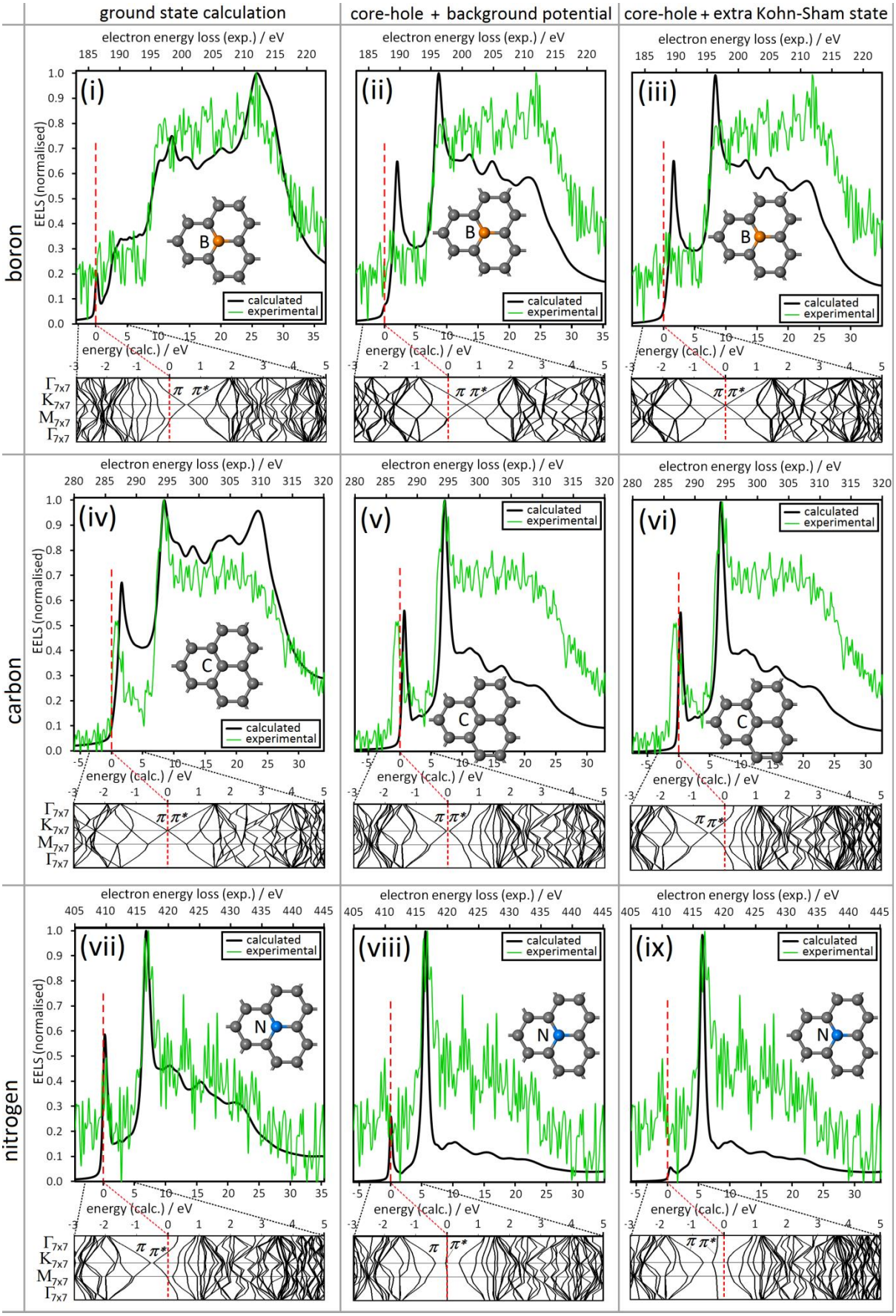

Figure 1 *Atomically-resolved background-subtracted experimental K-edge EEL spectra (green lines) recorded using aberration-corrected STEM for single substitutional B and N atoms in graphene as well as for pure*

graphene, with theoretical spectra (solid black lines) overlaid. Band structure plots calculated at three levels of theoretical approximation using 7x7 supercells are provided below each set of spectra. All theoretical spectra were rigidly translated along the energy axis to achieve the best-fit to the experimental curves. The 196th and 197th bands are identified as the π and π bands throughout. The theoretically calculated Fermi energy is defined as zero on the energy (calc.) axis and is indicated by the red dashed line. Combined plots for B (i) ground state, (ii) core-hole with neutralising background potential, (iii) core-hole with neutralising extra Kohn-Sham state. (iv)-(vi) Similar plots for C and (vii)-(ix) similar plots for N.*

B. Theory/experiment comparison

Overall, the theoretical ground state *K* edge spectra provide a better match to the experimental data compared to their core-hole counterparts which are unreliable and system-sensitive. The improvement in accuracy achieved as a result of using the ground state instead of a core-hole is significant for N as shown in Figures 1 (vii) - (ix), insignificant for C as shown in Figures 1 (iv) - (vi), but *critical* for B as shown in Figures 1 (i) - (iii). The task in this section, therefore, is to assess the various factors that lead to this result. A detailed and self-contained analysis of the calculation outputs without reference to the experimental data is given separately in section III C. Theoretical spectra using a half core-hole (Slater transition state) are given in the Supplementary Information.

On the energy axis, all N and C core-hole spectra underestimate the energy difference between the π* and σ* peaks, with the ground state spectra giving a slight improvement (C) or an excellent match (N) in this energy difference. As for intensities, both core-hole N spectra significantly underestimate the π* peak intensity compared to that of the σ* peak, whereas the ground state N spectrum only slightly overestimates the intensity of the π* peak compared to σ*; a slight improvement, therefore. The C core-hole spectra overestimate the π* intensity compared to the σ* peak intensity only slightly, and this is actually worsened in the ground state case. It is the case of B where the core-hole approximation fails critically, resulting in *qualitative* changes to the spectrum. The inclusion of a B core-hole causes the emergence of clearly identifiable π* and σ* spectral peaks in the theoretical B *K* spectrum which are completely absent in the ground state case, and indeed the recorded experimental data. The pivotal sensitivity of the theoretical B spectrum to the inclusion of a core-hole has an intuitive physical interpretation: the B nucleus, without a core-hole, is the only nucleus from all nine calculations which is significantly less electronegative than its C neighbours, and is therefore the only nucleus whose *K* edge spectrum has suppressed π* and σ* regions and culminates instead in a high-energy peak. A detailed and self-contained analysis of the calculation outputs without reference to the experimental data is given separately in section III C. In the Supplementary Information, we also provide plots showing how the theoretical spectra change with respect to the dopant's Mulliken charge by increasing the fractional number of 1*s* core-holes from zero to two in increments of 0.1*e*.

It is a good idea to consider the data in Figure 1 in the context of some established wisdom. It is well-known[86,87] that theoretical *K*-edge spectra are usually reasonably accurate in ground-state single-particle theory despite ignoring the effects of the electron self-interaction described in Hedin's "GW" approximation,[88] or two-particle effects as in the Bethe-Salpeter equation (BSE).[57] However, the question of whether to include a frozen core-hole within the single-particle DFT formalism is known to be highly dependent on the material. Metals, being well screened, are generally expected to be mostly unaffected by the creation of a beam-induced core-hole, so that EEL spectra of pure metals obtained experimentally will not exhibit any significant core-hole effects.[89-91] Expressed alternatively, the unoccupied states that are thought to exist under standard conditions in a metal are the same as, or similar to, the unoccupied states that are probed during the electron scattering event. This expectation is based on the notion that delocalised metallic states quickly screen the core-hole, leaving the unoccupied states - on which the spectrum depends - more or less unchanged. There is evidence that theoretical EELS calculated using single-particle DFT produces accurate results in the ground state for the Al *K*-edge[92] and Ni L_3-edge[93] and it is generally agreed that using a ground state calculation works well for metal EELS modelling.[89-91,94] (Luitz et al. published a counterexample to this trend with the Cu L_3-edge which was found to agree very well with experiment when using a half core-hole on all metal nuclei in the cell, better than a ground state calculation.[95]) Furthermore, the apparent adequacy of ground-state DFT for core-loss spectroscopy of doped graphene demonstrated in this paper is consistent with studies of Si-doped[44] and P-doped[96] graphene published by our group previously. A similar argument[77] can be made for, for example, anions in ionic insulators, whose intrinsic, localised excess electron density is expected to screen the core-hole effectively. This is in contrast to cations which are more exposed due to their intrinsic deficit of electron density and usually need a theoretical core-hole treatment for an accurate experimental match.

For metals, a comparison between two theoretically-calculated EEL spectra, one with a core-hole and one without, gives immediate insight because the two calculations can be compared. If the two theoretical spectra are similar and they both accurately match the experiment, then it can be said that the calculations accurately describe the metallic screening in the material. If the two theoretical spectra are *not* similar and the ground state spectrum gives a better match, it follows that the core-hole calculation does not accurately describe the metallic screening. It is important to remark at this point that the exotic systems studied in this work - single, isolated atomic-sized defects in a covalently-bonded 2D semimetal with a highly delocalised π network - cannot necessarily be described in a valid way by simply adopting the terminology conventionally used for bulk metals,

or for that matter, bulk insulators. Nevertheless, considering the highly conductive and delocalised π electrons in graphene, the ground state spectra Figure 1 which show mostly good agreement with experimental results are clear evidence that the sample probed in the microscope is behaving like a metal with respect to core-hole screening, in agreement with the existing body of literature regarding theoretical single-particle DFT EELS of metals.

As for the failure of the core-hole approximation for this system, Rez and Muller have noted[77] that the frozen core-hole approximation tends to exaggerate the effects of the core-hole when used in periodic supercells, and the results in this work appear to be evidence of this. In contrast to what would be expected for a material with delocalised and highly conductive states such as graphene, the theoretical spectra in Figure 1 show that inserting a frozen core-hole does cause the unoccupied states and the corresponding spectrum to change significantly. This is despite the supercells' large size, relaxed geometries and converged spectra. This mismatch of the calculation outputs with the conventional understanding of metallic core-hole screening in real laboratory samples discussed above, and of course the mismatch with the experimental data, should be taken as an indication that the final electronic states calculated using the frozen core-hole approximation in single-particle DFT simply do not give a realistic description of the states being probed in the microscope. To go some way to corroborating this finding, we have calculated *K*-edge spectra using CASTEP on pure bulk Al using an identical methodology and compared them with a published experimental spectrum[97] shown in Figure 2. While the ground state Al *K*-edge matches well at the edge onset, the half core-hole and full core-hole calculations show a progressive overestimation of the relative intensity at the onset compared to the experiment, with the intensity in the higher energy regions being progressively underestimated, thereby showing similar behaviour to that of the theoretical doped graphene spectra in Figure 1. Thus, while the ground state approximation has its limitations, we conclude that the frozen core-hole approximation should be regarded as an *ad hoc* modification which causes the models considered in this work to diverge away from reality, rather than converging towards it. In any case, single-particle DFT EELS modelling is not perfect,[98] and we expect that accounting for core-hole effects *a priori* by using the GW or BSE formalisms would be likely to improve the theory/experiment match compared to the ground-state, although the computational cost of such calculations with large supercells is at present prohibitive.

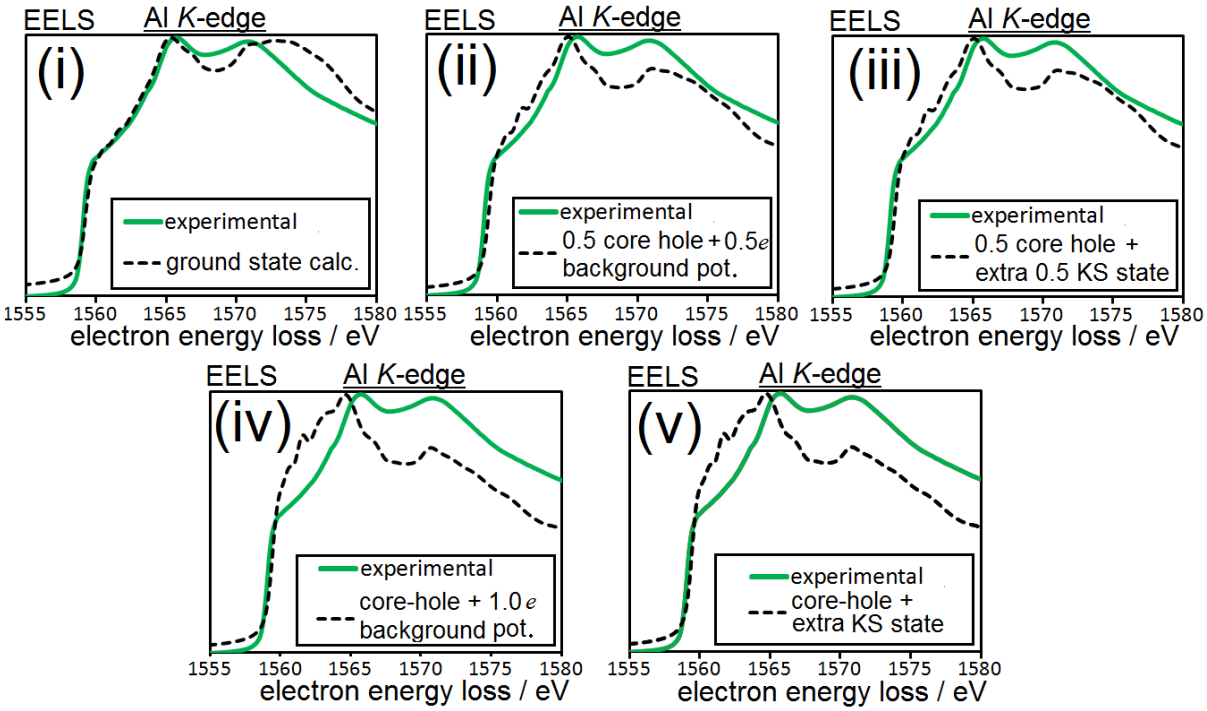

Figure 2 *Aluminium K-edge EEL spectrum compared with published experimentally-obtained X-ray absorption spectrum.*[97] *Calculation was carried out using identical calculation parameters (but without TS van der Waals corrections*[70]*) to the main calculations.*

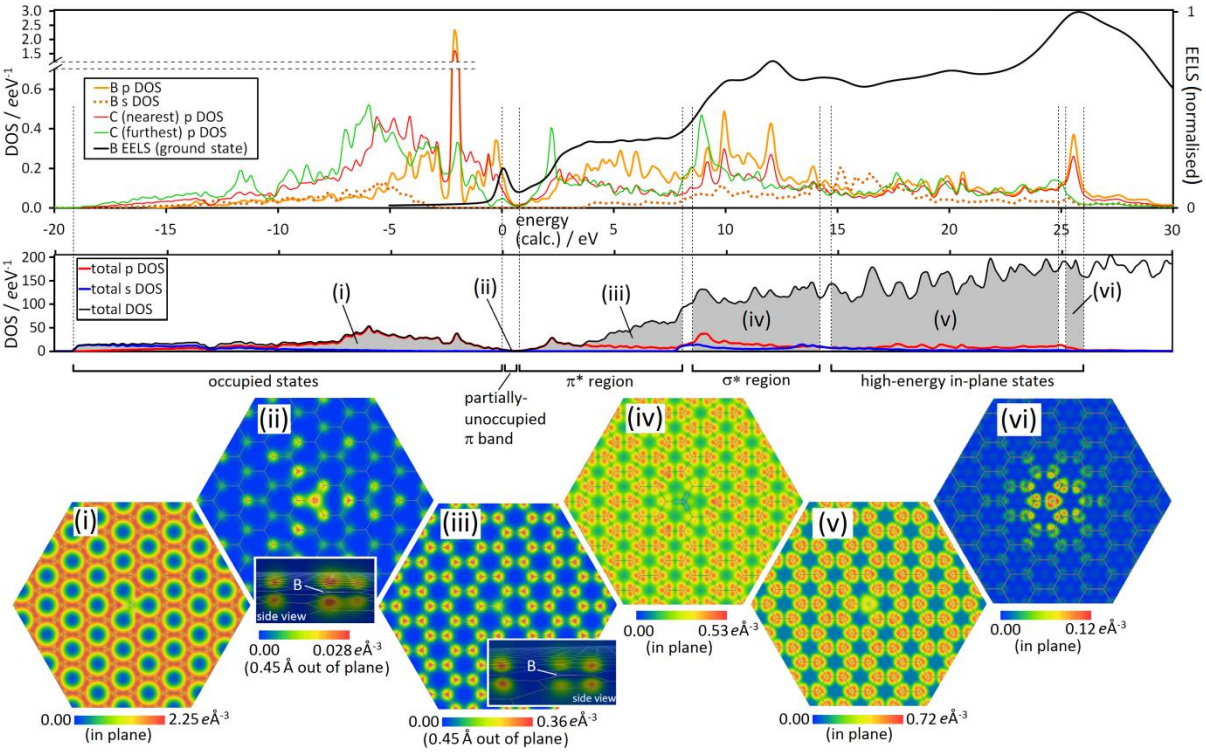

Figure 3 *Combined theoretical DOS/EELS plot for a substitutional B dopant in a ground state calculation with electron density plots in the Wigner-Seitz cell of (i) the occupied density in the ground state, (ii) the density lying solely in the partially-occupied π band corresponding to the filling of the p-type hole localised on the B, (iii) the out-of-plane π* states of p_z character with a density deficit on the B, (iv) the in-plane σ* states of antibonded (60°-rotated) sp^2 character with a deficit on the B, (v) the high-energy in-plane states with a deficit on the B and (vi) the high-energy in-plane B-localised states causing the theoretical B EELS peak at ~26 eV.*

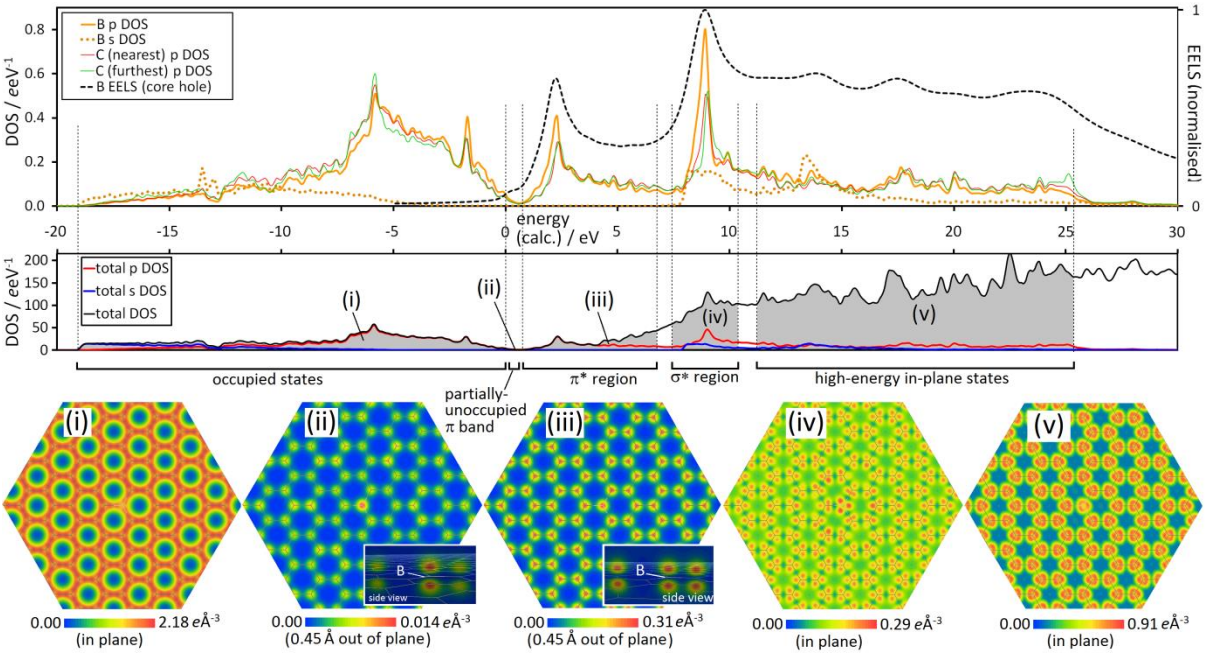

Figure 4 *Combined theoretical DOS/EELS plot for a substitutional B dopant with a B core-hole neutralised by a background potential with electron density plots of (i) the occupied density with the core-hole, (ii) the density from the partially-occupied π band which is more evenly distributed through the cell than its ground-state counterpart in Figure 3, (iii) the out-of-plane π* states of p_z character with a slight excess on the B, (iv) the in-plane σ* states of antibonded (60°-rotated) sp^2 character with a slight excess on the B and (v) the high-energy*

in-plane states with a very subtle deficit on the B. Note that there is no counterpart to the high energy B-localised state from Figure 3 (vi).

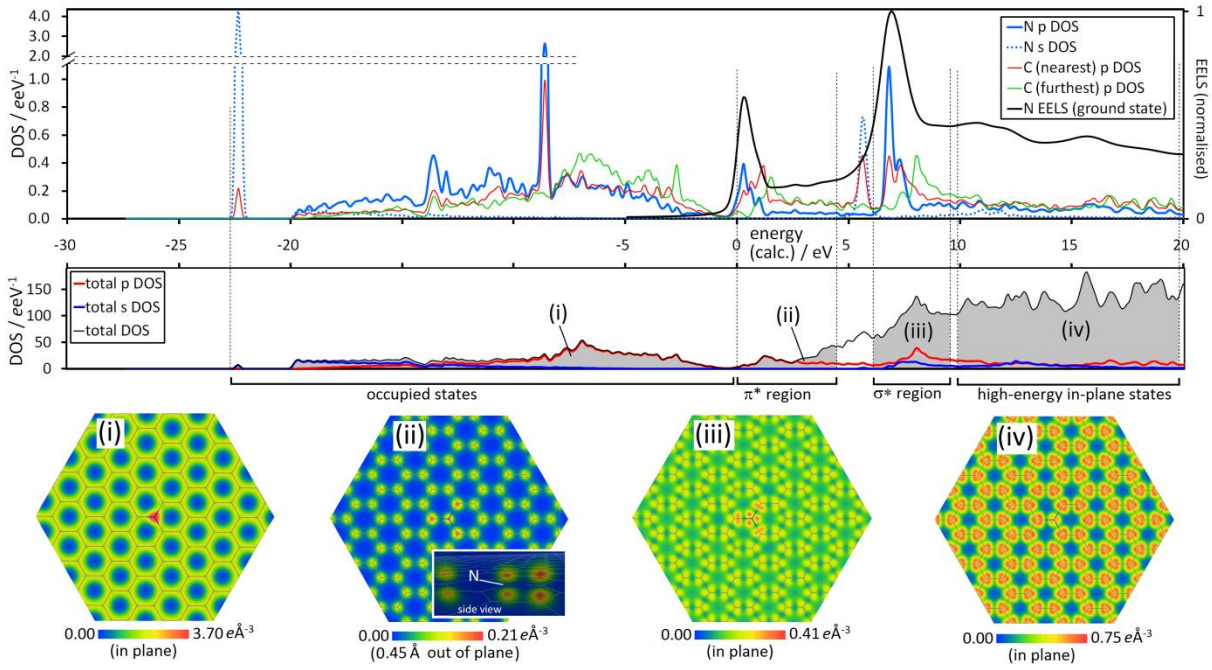

Figure 5 *Combined theoretical DOS/EELS plot for a substitutional N dopant in the ground state with electron density plots of (i) the occupied density in the ground state, (ii) the out-of-plane π* states of p_z character with a slight excess on the N and an excess on nearest-neighbour C nuclei, (iii) the in-plane σ* states of antibonded (60°-rotated) sp^2 character with a significant excess on the N and (iv) the high-energy in-plane states with a deficit on the N.*

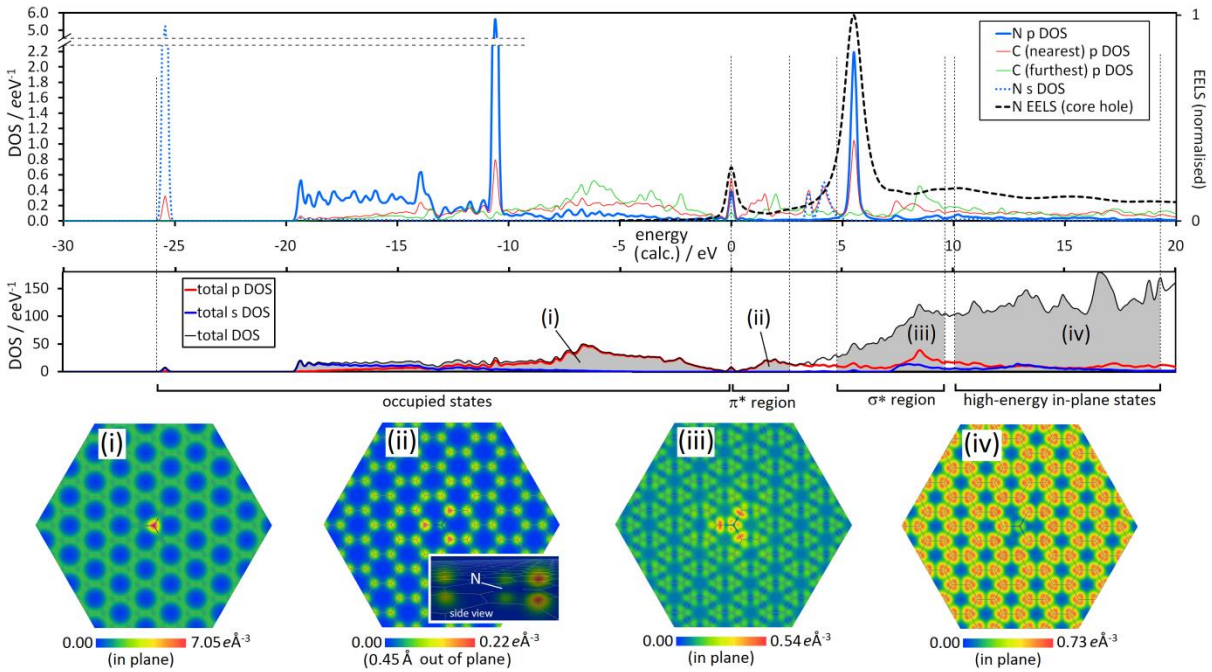

Figure 6 *Combined theoretical DOS/EELS plot for a substitutional N dopant with a core-hole neutralised by a background potential and electron density plots of (i) the occupied density with significant core-hole screening, (ii) the out-of-plane π* states of p_z character with a deficit on the N and a significant excess on nearest-neighbour C nuclei, (iii) the in-plane σ* states of antibonded (60°-rotated) sp^2 character with a significant excess on the N and (iv) the high-energy in-plane states with a significant deficit on the N.*

C. Self-contained theoretical analysis of calculated spectra

In this section the ground state and core-hole (with background potential) approximations are selected for detailed analysis for the cases of B (Figures 3 and 4) and N (Figures 5 and 6). The theoretical EEL spectra shown in Figures 3, 4, 5 and 6 are the same as those shown in Figures 1 (i), (ii), (vii) and (viii) respectively. Combined DOS/EELS plots with electron density images are provided in order to clearly illustrate the characteristics of the states underlying the theoretical spectra, with a view to gain a better understanding of the states being probed experimentally. The projected DOS of the dopant, nearest C and furthest C give some helpful insight into the electronegativity of each nucleus by showing the energies at which DOS peaks occur at varying distances from the dopant. The hexagonal panels within Figures 3 - 6 show (in addition to the occupied electron density) the electron density found by populating all unoccupied bands in the Wigner-Seitz cell (centered on the dopant) lying within a selected energy window above the Fermi energy. These energy windows were iteratively optimised according to the visual appearance of the states, and they form the basis for the denominations into π* states (out-of-plane), σ* states (in-plane) and higher-energy states (in-plane) indicated on each of the DOS plots. The reader should note that the density panels are not absolutely comparable due to the varying colour scales.

The ground state B *K* edge spectrum in Figure 3 shows a small π peak immediately above the Fermi energy due to the partially occupied π band whose density is highly localised on the B nucleus. This represents the filling of the *p*-type hole in the form of a p_z-like state in the partially occupied π band straddling the Fermi energy. The spectrum also shows suppressed π* and σ* peaks owing to the lesser electronegativity of the B nucleus compared to its C neighbours, and finally a high-energy in-plane state localised very strongly on the B nucleus at about 26 eV above the Fermi energy. The large energy barrier required to overcome the lesser attraction of the B nucleus causes the spectrum to culminate in the high-energy peak at 26 eV, which, when combined with the suppressed π* and σ* states at lower energy, gives rise to the unusual B *K* edge spectrum which matches the experimental spectrum quite convincingly. The B *p* DOS peaks in the π* and σ* regions occur at higher energies than the clearly identifiable furthest C *p* DOS peaks, which confirms the lesser electronegativity of B compared to C. Some antibonding states between the B and nearest-C is also evident from the coincidence of sharp *p* DOS peaks, especially in the σ* region. The effect of including a core-hole on the B nucleus, as shown in Figure 4, is to increase its electronegativity. This eliminates the high-energy state found at +26 eV in the ground state case

because there is no such energy barrier to be overcome with a core-hole present. In fact, all states of character π* and σ* now lie in approximately the same energy range whether they are localised on B or C, which is evident from the more subtle differences in the projected DOS and electron density. The EELS π peak is suppressed to a subtle shoulder corresponding to a state which is much less localised on the B than in the ground state case. Neutralising the core-hole using an extra Kohn-Sham state as in Figure 1 (iii) completely suppresses the π peak due to the π band now being fully occupied. The overall result of including the core-hole is thus the emergence of clearly identifiable π* and σ* EELS peaks in the B *K* edge spectrum since the core-hole makes the B nucleus approximately carbon-like.

The N *K* edge ground state spectrum in Figure 5 exhibits a clear π* peak due to p_z-like states localised on the N and its nearest neighbours, and a σ* peak due to states consistent with antibonded (60°-rotated) sp^2-like orbitals strongly localised on the N nucleus. Note that the N *p* DOS peaks in the π* and σ* regions now occur at lower energies than those of the C due to N's higher electronegativity (with some nearest-neighbour antibonding again evident), in contrast to the B case in Figure 3. Figure 6 shows that the effect of including a N core-hole is to exacerbate the effects caused by the difference in the electronegativity of N and C: the π* and σ* peaks of the N *K* edge spectrum now occur at lower energies with the core-hole, and the energy difference between the *p* DOS peaks of the N and nearest C is now higher. The σ* peak in particular is attributable to a very sharp N *p* DOS peak at about 5.5 eV where the electron density localisation on N has been enhanced by the core-hole. Interestingly, the N EELS π* peak is actually *suppressed* by including the core-hole. This can be rationalised to some extent by comparing Figures 5 (i) and 6 (i), which reveals that the core-hole causes the occupied electron density to accumulate more strongly around the N, resulting in nuclear screening that is sufficiently strong to make the N nucleus less energetically attractive than the nearest neighbour C nuclei. This is corroborated by the *p* DOS peak of the N directly on the Fermi energy which is lower in intensity than the *p* DOS peak of the nearest-C with which it coincides. If the core-hole is instead neutralised using an extra Kohn-Sham state, corresponding to Figure 1 (ix), then this π* peak is further suppressed since the first π* band is then fully occupied.

IV. CONCLUSIONS

It was found that the theoretical core-hole approximation in single-particle DFT EELS is significantly less successful in predicting atomically-resolved *K*-edge spectra in B- and N-doped graphene than the simpler ground state approximation, and fails to offer any improvement of the C *K*-edge in pure graphene. We conclude

that the frozen core-hole approximation is not a realistic description of the core-hole and should be discarded in favour of the ground state approximation for this system. To confirm the robust nature of the calculations, a detailed and independent analysis of the theoretical results for the B and N cases under both approximations was given which allows for an understanding and visual comparison of the calculated quantum states, identified and discussed using the conventional terminology of sp^2-bonded materials. Modern electron microscopes are now sufficiently advanced to push the validity of the approximations used in theoretical electronic structure calculations, and there is evidently a growing need to increase the efficiency of more advanced computational schemes using the GW and BSE formalisms, among others.

VI. ACKNOWLEDGEMENTS

T. P. H. would like to thank the Engineering and Physical Sciences Research Council (EPSRC) for the Doctoral Prize Fellowship and SuperSTEM which funded this research. SuperSTEM is the UK EPSRC National Facility for aberration-corrected STEM. T.S. acknowledges funding from the Austrian Science Fund (FWF) via project P 28322-N36. Computational work was undertaken using the high performance scientific computing facilities ARC1 and ARC2 at the University of Leeds.

V. REFERENCES

[1]K. S. Novoselov, A. K. Geim, S. V. Morozov, D. Jiang, Y. Zhang, S. V. Dubonos, I. V. Grigorieva, and A. A. Firsov *Science* ***306****, 666 (2010)*

[2]C. Berger, Z. Song, T. Li, X. Li, A. Y. Ogbazghi, R. Feng, Z. Dai , A. N. Marchenkov, E. H. Conrad , P. N. First, and W. A. de Heer *Journal of Physical Chemistry B*, ***108,*** *19912 (2004)*

[3]A. K. Geim and K. S. Novoselov *Nature Materials* ***6****, 183 (2007)*

[4]A. Das, S. Pisana, B. Chakraborty, S. Piscanec, S. K. Saha, U. V. Waghmare, K. S. Novoselov, H. R. Krishnamurthy, A. K. Geim, A. C. Ferrari, and A. K. Sood *Nature Nanotechnology* ***3****, 210 (2008)*

[5]Y.-M. Lin, K. A. Jenkins, A. Valdes-Garcia, J. P. Small, D. B. Farmer, and P. Avouris *Nano Lett.* ***9****, 422 (2009)*

[6]Y.-M. Lin, C. Dimitrakopoulos, K. A. Jenkins, D. B. Farmer, H.-Y. Chiu, A. Grill, and Ph. Avouris *Science* ***327****, 662 (2010)*

[7]R. Chenga, J. Baia, L. Liaob, H. Zhoub, Y. Chena, L. Liub, Y.-C. Lina, S. Jiangb, Y. Huanga, and X. Duan *Proceedings of the National Academy of Sciences* ***109****, 11588 (2012)*

[8]Y.-W. Son, M. L. Cohen, and S. G. Louie *Physical Review Letters* ***97****, 216803 (2006)*

[9]M. Y. Han, B. Özyilmaz, Y. Zhang, and P. Kim *Physical Review Letters* ***98****, 206805 (2007)*

[10]Y. Zhang, T.-T. Tang, C. Girit, Z. Hao, M. C. Martin, A. Zettl, M. F. Crommie, Y. R. Shen, and F. Wang *Nature* ***459****, 820 (2009)*

[11]T. Ohta, A. Bostwick, T. Seyller, K. Horn, and E. Rotenber *Science* ***313****, 951 (2006)*

[12]Z. H. Ni, T. Yu, Y. H. Lu, Y. Y. Wang, Y. P. Feng, and Z. X. Shen *ACS Nano* ***2****, 2301 (2008)*

[13]V. M. Pereira, A. H. Castro Neto, and N. M. R. Peres *Physical Review B* ***80****, 045401 (2009)*

[14]F. Guinea, M. I. Katsnelson, and A. K. Geim *Nature Physics* ***6****, 30 (2010)*

[15]G. Liu, S. Ahsan, A. G. Khitun, R. K. Lake, and A. A. Balandin *Journal of Applied Physics* ***114****,154310 (2013)*

[16]C. R. Dean, A. F. Young, I. Meric, C. Lee, L. Wang, S. Sorgenfrei, K. Watanabe, T. Taniguchi, P. Kim, K. L. Shepard, and J. Hone *Nature Nanotechnology* ***5****, 722 (2010)*

[17] L. Liao,Y.-C. Lin, M. Bao, R. Cheng, J. Bai, Y. Liu, Y. Qu, K. L. Wang, Y. Huang, and X. Duan Nature **467**, 305 (2010)

[18]Y.-M. Lin, A. Valdes-Garcia, S.-J. Han, D. B. Farmer, I. Meric, Y. Sun, Y. Wu, C. Dimitrakopoulos, A. Grill, P.Avouris, and K.A. Jenkins *Science* ***332****, 1294 (2011)*

[19]S.-J. Han, A. V. Garcia, S. Oida, K. A. Jenkins, and W. Haensch *Nature Communications* ***5****, 3086 (2014)*

[20]B. Radisavljevic, A. Radenovic, J. Brivio, V. Giacometti, and A. Kis *Nature Nanotechnology* ***6****, 147 (2011)*

[21]L. Li, Y. Yu, G. J. Ye, Q. Ge, X. Ou, H. Wu, D. Feng, X. H. Chen, and Y. Zhang *Nature Nanotechnology* ***9****, 372 (2014)*

[22]M. Buscema, D. J. Groenendijk, S. I. Blanter, G. A. Steele, H. S. J. van der Zant, and A. Castellanos-Gomez *Nano Letters* **14**, 3347 (2014)

[23]*D*. Hanlon, C. Backes, E. Doherty, C. S. Cucinotta, N. C. Berner, C. Boland, K. Lee, A. Harvey, P. Lynch, Z. Gholamvand, S. Zhang, K. Wang, G. Moynihan, A. Pokle, Q. M. Ramasse, N. McEvoy, W. J. Blau, J. Wang, G. Abellan, F. Hauke, A. Hirsch, S. Sanvito, D. D. O'Regan, G. S. Duesberg, V. Nicolosi, and J. N. Coleman, *Nature Communications* ***6****, 8563 (2015)*

[24]Y, Li, Y, Zha, H. Cheng, Y. Hu, G. Shi, L. Dai, and L. Qu *Journal of the American Chemical Society* ***134****, 15 (2012)*

[25]L. Zhang and Z. Xia *The Journal of Physical Chemistry C* ***115****, 11170 (2011)*

[26]L. Qu, Y. Liu, J.-B. Baek, and L. Dai *ACS Nano* ***4****, 1321 (2010)*

[27]L. Lai, J. R. Potts, D. Zhan, L. Wang, C. K. Poh, C. Tang, H. Gong, Z. Shen, J. Linc, and R. S. Ruoff *Energy, and Enviromental Science* ***5****, 7936 (2012)*

[28]A. L. M. Reddy, A. Srivastava, S. R. Gowda, H. Gullapalli, M. Dubey, and P. M. Ajayan *ACS Nano*, ***4****, 6337 (2010)*

[29]H. M. Jeong, J. W. Lee, W. H. Shin, Y. J. Choi, H. J. Shin, J. K. Kang, and J. W. Choi *Nano Letters* ***11****, 2472 (2011)*

[30]Z. Wen, X. Wang, S. Mao, Z. Bo, H. Kim, S. Cui, G. Lu, X. Feng, and J. Chen *Advanced Materials* ***24****, 5610 (2012)*

[31]Y. Wang, Y. Shao, D. W. Matson, J. Li, and Y. Lin *ACS Nano* ***4****, 1790 (2010)*

[32]Z.-H. Sheng, H.-L. Gao, W.-J. Bao, F.-B. Wang, and X.-H. Xia *Journal of Materials Chemistry* ***22****, 390 (2012)*

[33]T. Lin, F. Huang, J. Lianga, and Y. Wang *Energy & Environmental Science* ***4****, 862 (2010)*

[34]L. Niu, Z. Li, W. Hong, J. Sun, Z. Wang, L. Ma, J. Wang, S. Yang *Electrochimica Acta* ***108****, 666 (2013)*

[35]T. B. Martins, R. H. Miwa, A. J. R. da Silva, and A. Fazzio *Physical Review Letters* ***98****, 196803 (2007)*

[36]U. Bangert, W. Pierce, D. M. Kepaptsoglou, Q. M. Ramasse, R. Zan, M. H. Gass, J. A. Van den Berg, C. B. Boothroyd, J. Amani, and H. Hofsäss *Nano Letters* ***13****, 4902 (2013)*

[37]D. Kepaptsoglou, T. P. Hardcastle, C. R. Seabourne, U. Bangert, R. Zan, J. A. Amani, H. Hofsäss, R. J. Nicholls, R. M. D. Brydson, A. J. Scott, and Q. M. Ramasse *ACS Nano* ***9****, 11398 (2015)*

[38]P. Hohenberg and W. Kohn *Physical Review* ***136****, B864 (1964)*

[39]W. Kohn and L. J. Sham *Physical Review* ***140****, A14433 (1965)*

[40]R. J. Nicholls, A. T. Murdock, J. Tsang, J. Britton, T. J. Pennycook, A. Koós, P. D. Nellist, N. Grobert, and J. R. Yates *Nano Letters* **7**, 7145 (2013)

[41]J. H.Warner, Y.-C. Lin, K. He, M. Koshino, and K. Suenaga *ACS Nano* ***8****, 11806 (2014)*

[42]R. Arenal, K. March, C. P. Ewels, X. Rocquefelte, M. Kociak, A. Loiseau, and O. Stéphan *Nano Letters* ***14****, 5509 (2014)*

[43]Y.-C. Lin, P.-Y. Teng, C.-H. Yeh, M. Koshino, P.-W. Chiu, and K. Suenaga *Nano Letters* **15**, 7408 (2015)

[44]Q. M. Ramasse, C. R. Seabourne, D.-M. Kepaptsoglou, R. Zan, U. Bangert, and A. J. Scott *Nano Letters* ***13****, 4989 (2013)*

[45]J. Fink *Transmission electron energy-loss spectroscopy*. Chapter 7 in J. C. Fuggle and J. E. Inglesfield *Topics in Applied Physics Vol* ***69****: Unoccupied Electronic States, Springer, Berlin (1992)*

[46]E. Runge and E. K. U. Gross *Physical Review Letters* ***52****, 997 (1984)*

[47]J. Yan, J. Mortensen, K. W. Jacobsen, and K. S. Thygesen *Physical Review B* ***83****, 245122 (2011)*

[48]J. S. L. Adler *Physical Review* ***126****, 413 (1962)*

[49]J. N. Wiser *Physical Review* ***129****, 62 (1963)*

[50]V. U. Nazarov *New Journal of Physics* ***17****, 073018 (2015)*

[51]V. U. Nazarov *Physical Review B* ***93****, 035403 (2016)*

[52]Y. Liu, R. F. Willis, K. V. Emtsev, and T. Seyller *Physical Review B* ***78*** *201403 (2008)*

[53]T. Eberlein, U. Bangert, R. R. Nair, R. Jones, M. Gass, A. L. Bleloch, K. S. Novoselov, A. K. Geim and P. R. Briddon *Physical Review B* ***77****, 233406 (2008)*

[54]M. H. Gass, U.Bangert, A. L. Bleloch, P. Wang1, R. R. Nair, and A. K. Geim *Nature Nanotechnology* ***3*** *676 (2008)*

[55]S. C. Liou, C. S. Shie, C. H. Chen, R. Breitwieser, W. W. Pai, G. Y. Guo, and M. W. Chu *Physical Review B* ***91*** 045418 (2015)

[56]F. J. Nelson, J.-C. Idrobo, J. D. Fite , Z. L. Mišković, S. J. Pennycook, S. T. Pantelides, J. U. Lee, and A. C. Diebold *Nano Letters* ***14,*** *3827 (2014)*

[57]E. E. Salpeter and H. A. Bethe *Physical Review* ***84****, 1232 (1951)*

[58]H. Ehrenreich and M. H. Cohen *Physical Review* ***115****, 786 (1959)*

[59]R. F. Egerton *Electron Energy Loss Spectroscopy in the Electron Microscope, Springer, New York, (2011)*

[60]J. C. Slater and G. F. Koster *Physical Review* ***94****, 1498 (1954)*

[61]D. Sanchez-Portal, E. Artacho, and J. M. Soler *Solid State Communications* ***95****, 685 (1995)*

[62]M. D. Segall, R. Shah, C. J. Pickard, and M. C. Payne *Physical Review B* ***54****, 16317 (1996)*

[63]P. E. Blöchl *Physical Review B* ***50****, 17953 (1994)*

[64]S.-P. Gao, C. J. Pickard, A. Perlov, and V. Milman *Journal of Physics: Condensed Matter* ***21****, 104203 (2009)*

[65]S. J. Clark, M. D. Segall, C. J. Pickard, P. J. Hasnip, M. J. Probert, K. Refson, and M. C. Payne *Zeitschrift fuer Kristallographie* ***220****, 567 (2005)*

[66]C. J. Pickard *Ph.D. thesis, University of Cambridge, UK 1997*

[67]T. P. Hardcastle, C. R. Seabourne, R. Zan, R. M. D. Brydson, U. Bangert, Q. M. Ramasse, K. S. Novoselov, and A. J. Scott *Physical Review B* ***87****, 195430 (2013)*

[68]P. Trucano and R. Chen *Nature* ***258****, 136 (1975)*

[69]J. P. Perdew, K. Burke, and M. Ernzerhof *Physical Review Letters* ***77****, 3865 (1996)*

[70]A. Tkatchenko and M. Scheffler *Physical Review Letters* ***102****, 073005 (2009)*

[71]H. J. Monkhorst and J. D. Pack *Physical Review B* ***13****, 5188 (1976)*

[72]C. G. Broyden *IMA Journal of Applied Mathematics* ***6****, 76 (1970)*

[73]C. G. Broyden *IMA Journal of Applied Mathematics* ***6****, 222 (1970)*

[74]R. Fletcher *The Computer Journal* ***13****, 317 (1970)*

[75]D. Goldfarb *Mathematics of Computation* ***24****, 23 (1970)*

[76]D. F. Shanno *Mathematics of Computation* ***24****, 647 (1970)*

[77]Y.-C. Zhou, H.-L. Zhang, and W.-Q. Deng *Nanotechnology* ***24****, 225705 (2013)*

[78]T. Susi, D. J. Mowbray, M. P. Ljungberg, and P. Ayala *Physical Review B* ***91****, 081401(R)*

[79]V. Despoja, D. J. Mowbray, D. Vlahović, and L. Marušić *Physical Review B* ***86****, 195429 (2012)*

[80]J. C. Fuggle and J. E. Inglesfield *Topics in Applied Physics Vol* ***69****: Unoccupied Electronic States, Springer, Berlin (1992)*

[81]T. Mizoguchi, I. Tanaka, S.-P. Gao, and C. J. Pickard *Journal of Physics: Condensed Matter* ***21****, 104204 (2009)*

[82]A. J. Morris, R. J. Nicholls, C. J. Pickard, and J. R. Yates *Computer Physics Communications* ***185****, 1477 (2014)*

[83]J. R. Yates, X. Wang, D. Vanderbilt, and I. Souza *Physical Review B* ***75****, 195121 (2007)*

[84]Y. Xu, K. Zhang, C. Brüsewitz, X. Wu, and H. C. Hofsäss *AIP Advances* ***3****, 072120 (2013)*

[85]S. Casolo, R. Martinazzo, and G. F. Tantardini *The Journal of Physical Chemistry C* ***115****, 3250 (2011)*

[86]F. de Groot, A. Kotani *Core Level Spectroscopy of Solids,* eds. by D. D. Sarma, G. Kotliar and Y. Tokura, *Advances in Condensed Matter Science, Vol* ***6*** *CRC Press, Taylor & Francis, Boca Raton, London, New York, (2008)*

[87]G. Radtke and G. A. Botton *Scanning Transmission Electron Microscopy* by S. J. Pennycook, P. D. Nellist (eds.), *Springer, New York (2011)*

[88]L. Hedin *Physical Review* ***139****, A796 (1965)*

[89]P. Rez, J. R. Alvarez and C. Pickard *Ultramicroscopy* ***78****, 175 (1999)*

[90]P. Rez and D. Muller *Annual Review of Materials Research* ***38****, 535 (2008)*

[91]P. Rez, J. Bruley, P. Brohan, M. Payne and L. A. J. Garvie *Ultramicroscopy* ***59****, 159 (1995)*

[92]C. R. Seabourne, A. J. Scott, R. M. D. Brydson, and R. J. Nicholls *Ultramicroscopy* ***109****, 1374 (2009)*

[93]D. A. Muller, D. J. Singh, J. Silcox *Physical Review B* ***57****, 8181 (1998)*

[94]G. A. Botton, G. Y. Guo, W. M. Temmerman, and C. J. Humphreys *Physical Review B* ***54****, 1682 (1996)*

[95]J. Luitz, M. Maier, C. Hébert, P. Schattschneider, P. Blaha, K. Schwarz, and B. Jouffrey *The European Physical Journal B* ***21****, 363 (2001)*

[96]T. Susi, T. P. Hardcastle, H. Hofsäss, A. Mittelberger, T. J Pennycook, C. Mangler, R. D. Brydson, A. J. Scott, J. C. Meyer, and J. Kotakoski *2D Materials* ***4****, 021013 (2017)*

[97]A-.M. Flank *Aluminium X-ray absorption K-edge spectrum, CEMES & IMN Laboratories database, downloaded from http://eelsdb.eu*.

[98]P. Rez *Microscopy and Microanalysis* ***12*** *(Supp. 2), 108 (2006)*

SUPPLEMENTARY INFORMATION

Convergence of bond lengths with supercell size

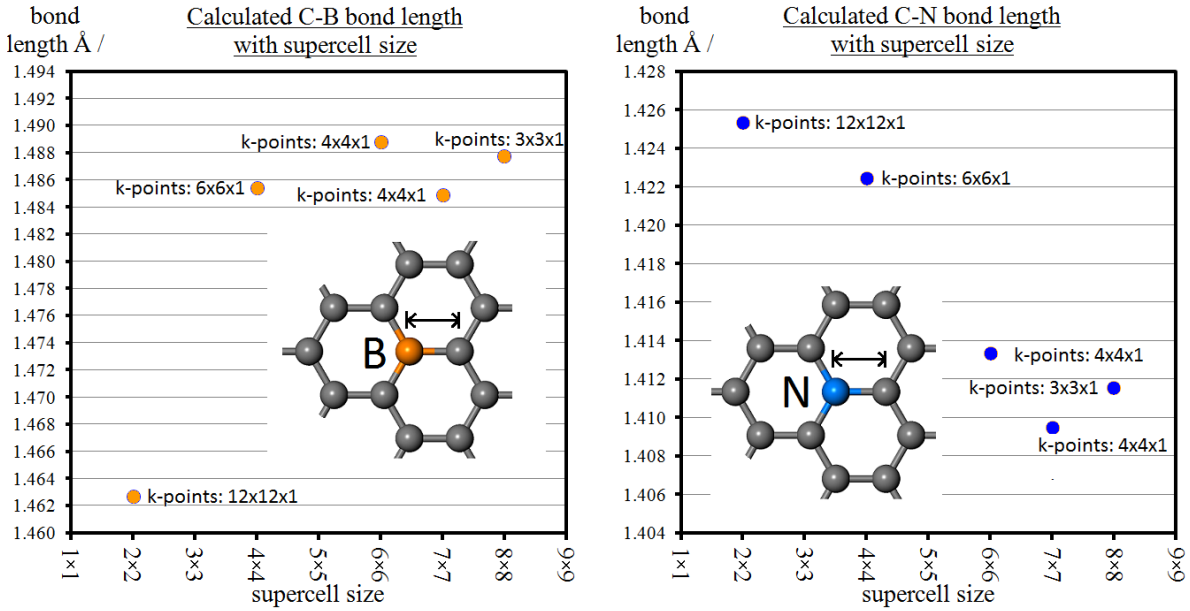

Fig. S.1. *Convergence of the bond length between each dopant and its nearest carbon neighbour with supercell size, calculated using the PBE+TS functional. The 7x7 cases break the trend slightly due to the difference in k-point spacings.*

bond *cell size*	**2x2**	**4x4**	**6x6**	**7x7**	**8x8**
C(nearest) to N	1.42536 Å	1.42248 Å	1.41335 Å	1.40951 Å	1.41156 Å
C(nearest) to B	1.46275 Å	1.48544 Å	1.48885 Å	1.48497 Å	1.48782 Å

Table. S.1. *Data from Fig. S.1.*

Convergence of *K* edges with supercell size

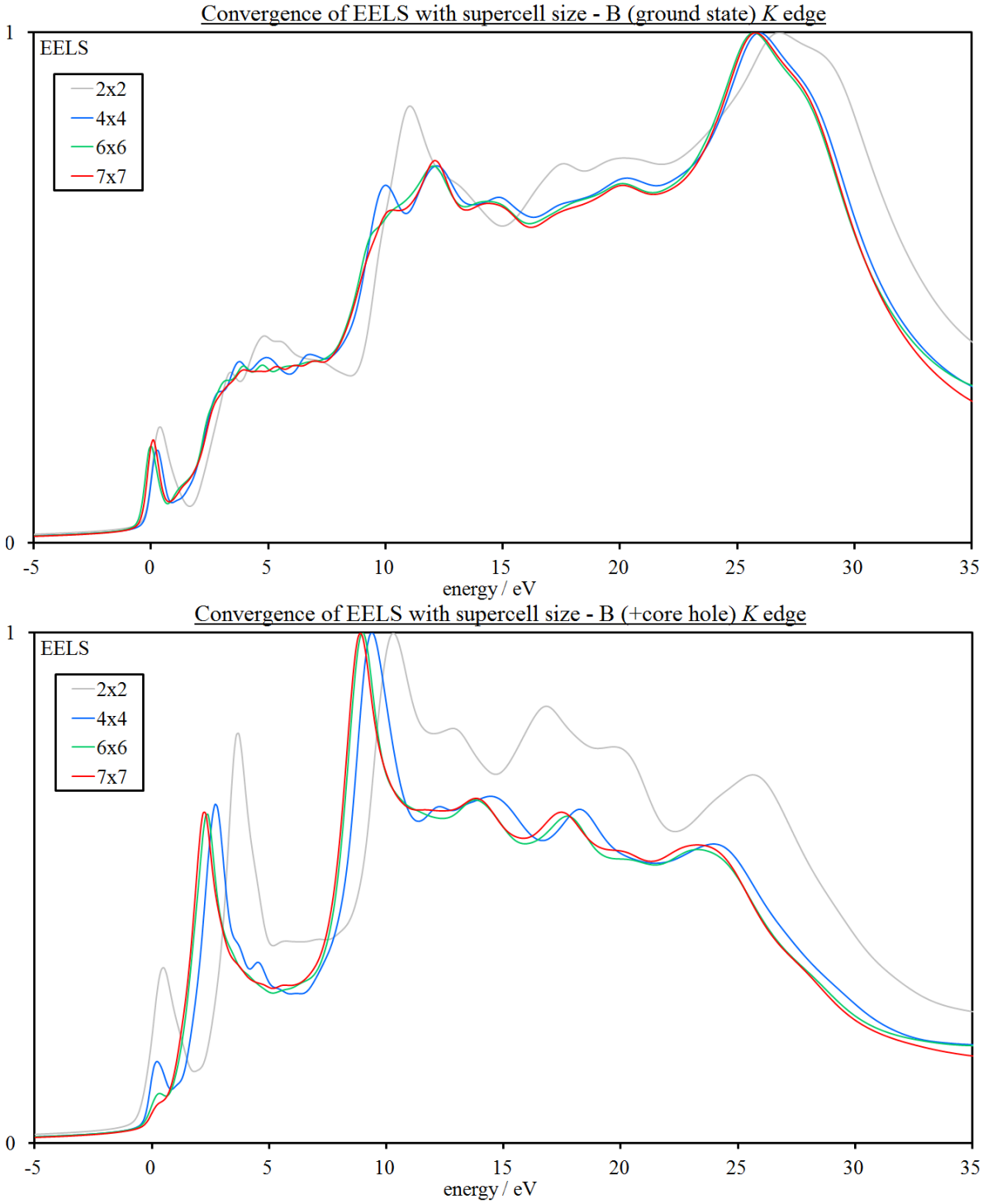

Fig. S.2. *Convergence of B K edge with supercell size for ground state and core-hole calculations.*

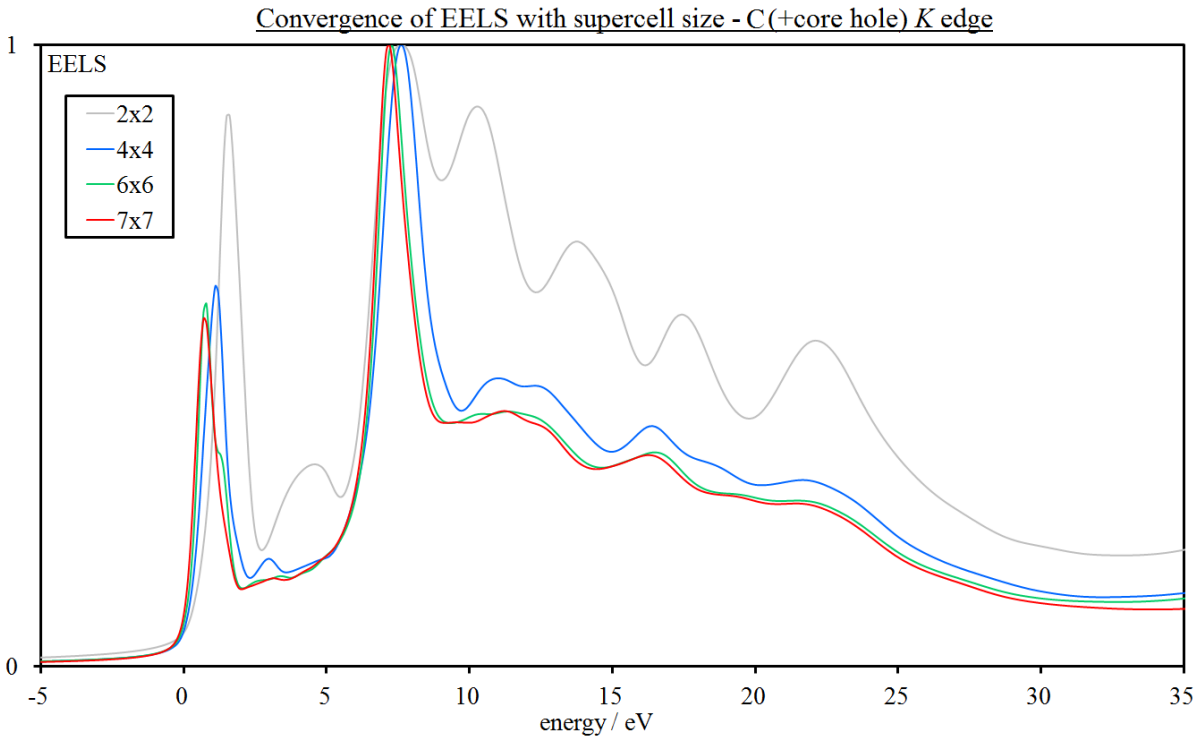

Fig. S.3. *Convergence of C K edge with supercell size for core-hole calculation.*

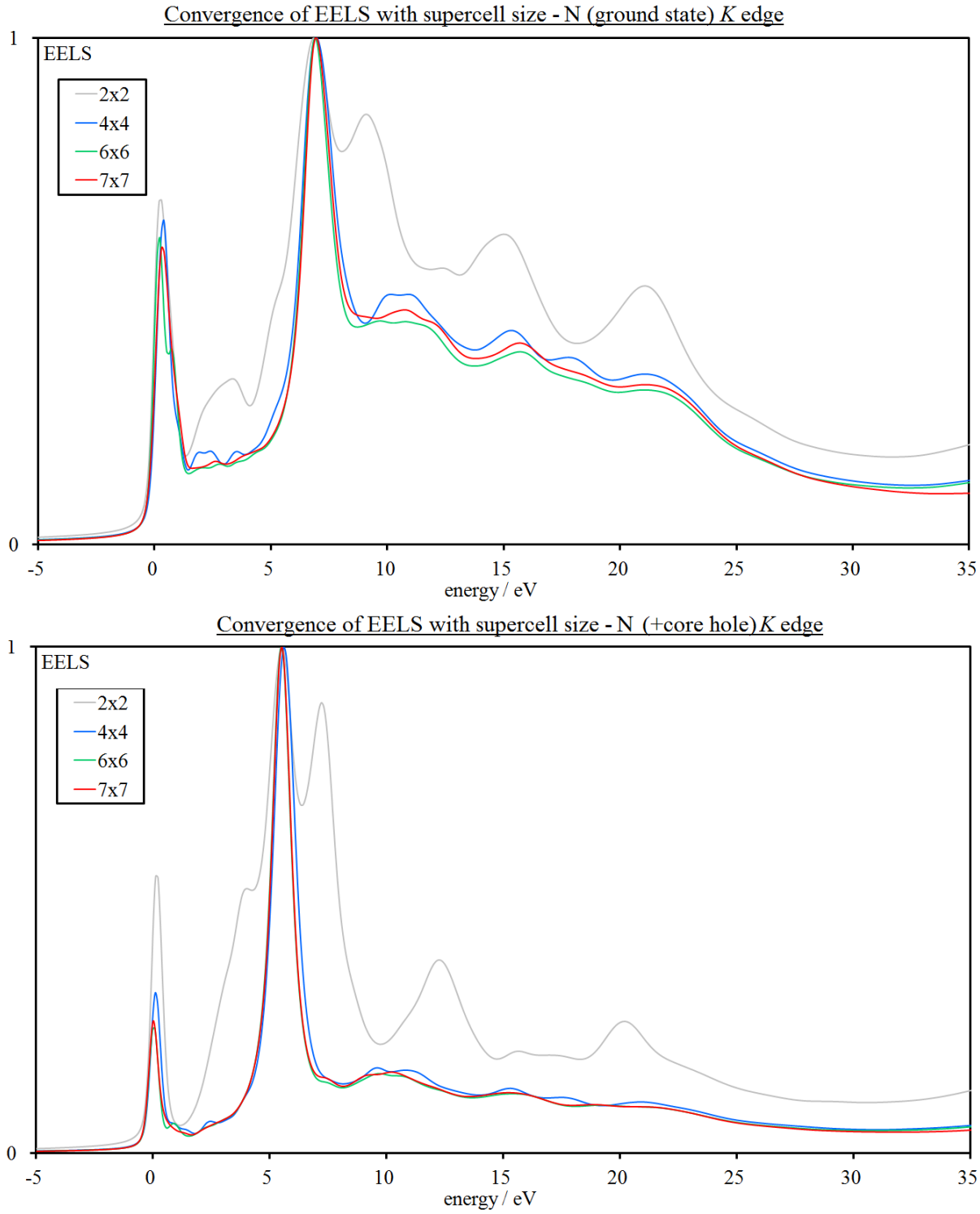

Fig. S.4. *Convergence of N K edge with supercell size for ground state and core-hole calculations.*

Convergence of *K* edges with vacuum thickness: boron

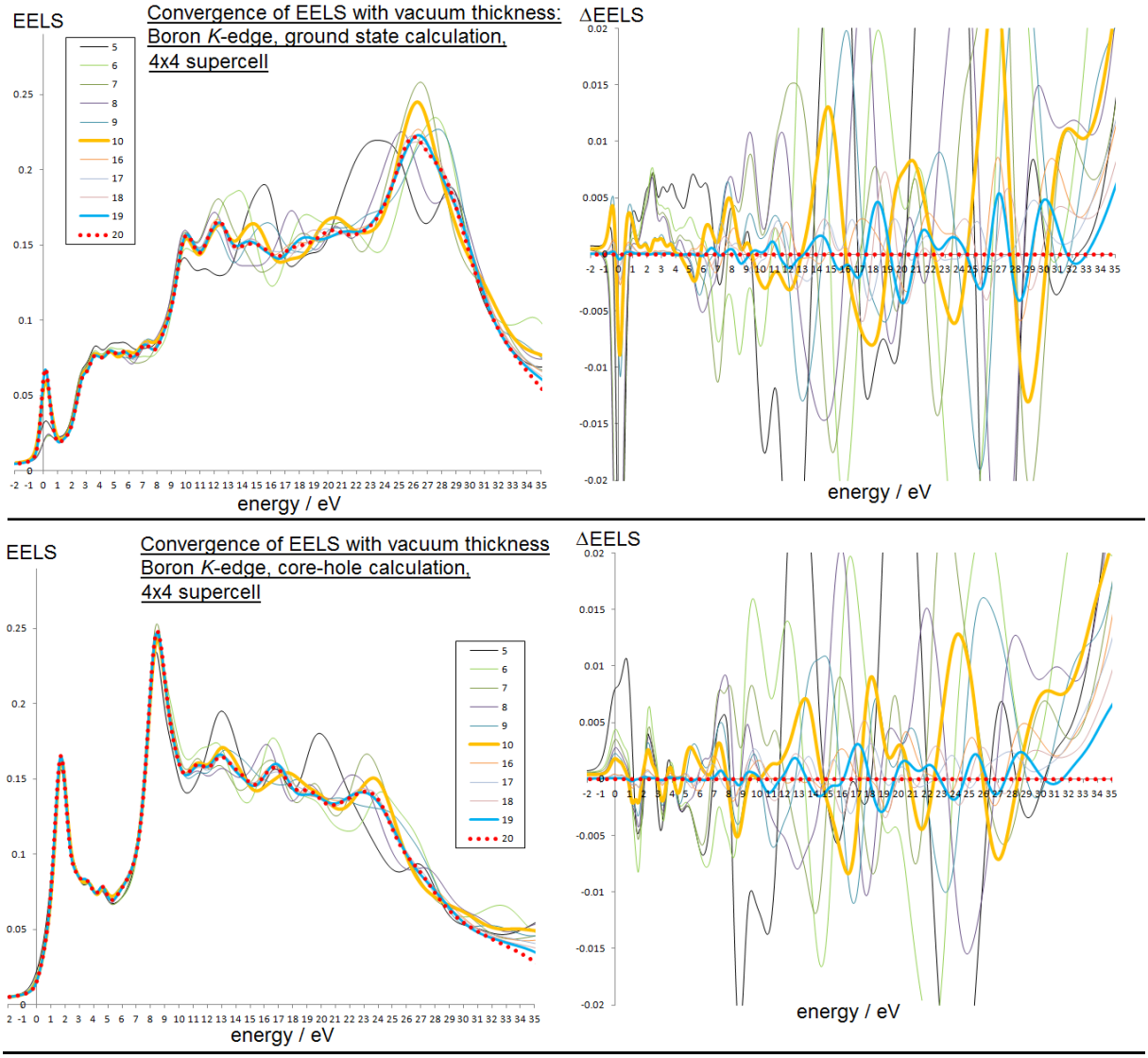

Fig. S5. ***Left panels:*** *Convergence of B K edge with vacuum thickness using 4×4 supercells. The spectra are volume-normalised.* ***Right panels:*** *The differences between each spectrum and the spectrum calculated with a 20Å vacuum. Note that since 4×4 supercells were used for the vacuum convergence tests, these spectra are not fully converged with respect to in-plane supercell dimensions.*

Convergence of *K* edges with vacuum thickness: nitrogen

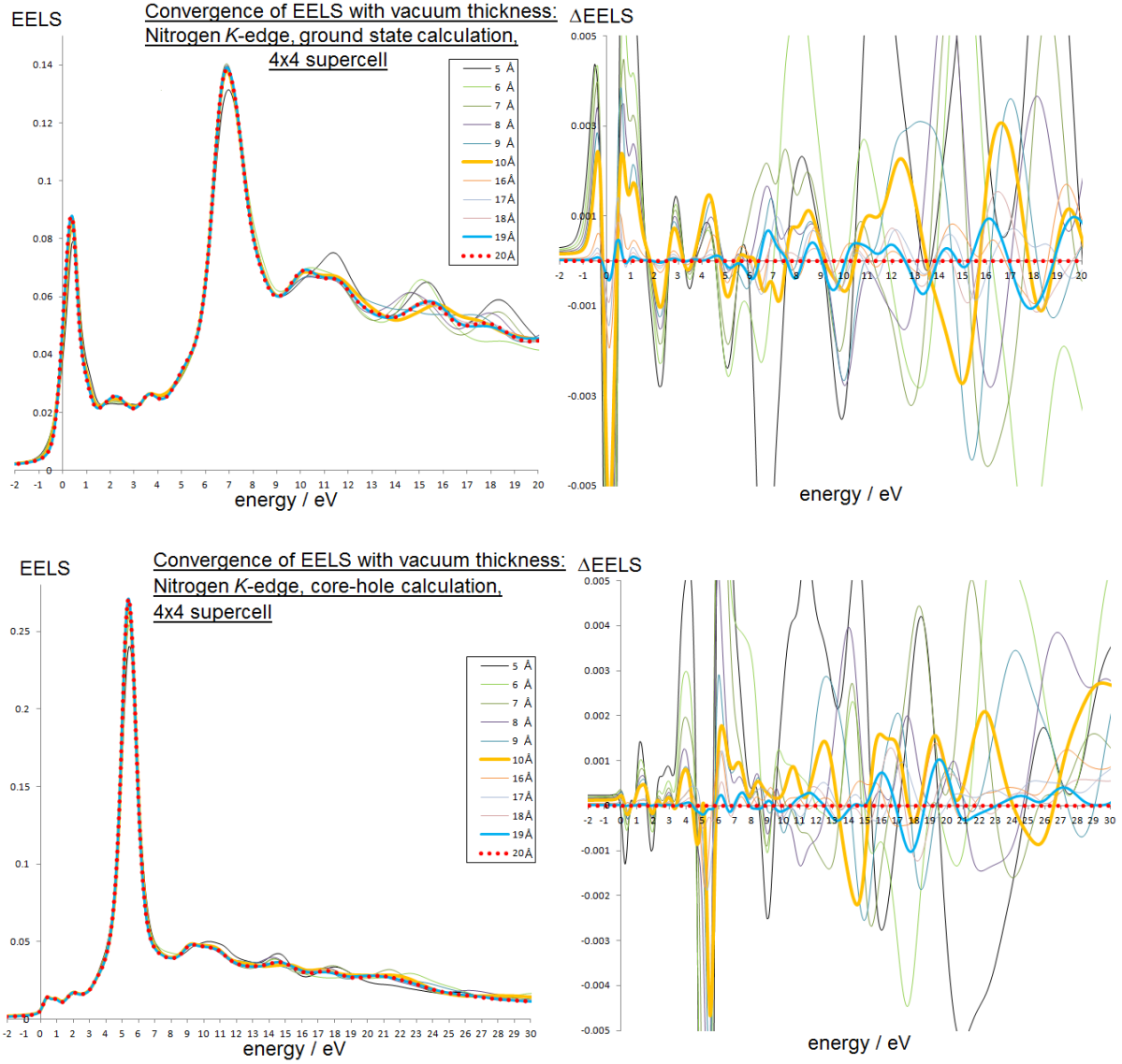

Fig. S.6. ***Left panels:*** *Convergence of N K edge with vacuum thickness using 4×4 supercells. The spectra are volume-normalised.* ***Right panels:*** *The differences between each spectrum and the spectrum calculated with a 20Å vacuum. Note that since 4×4 supercells were used for the vacuum convergence tests, these spectra are not fully converged with respect to in-plane supercell dimensions.*

k-points grids

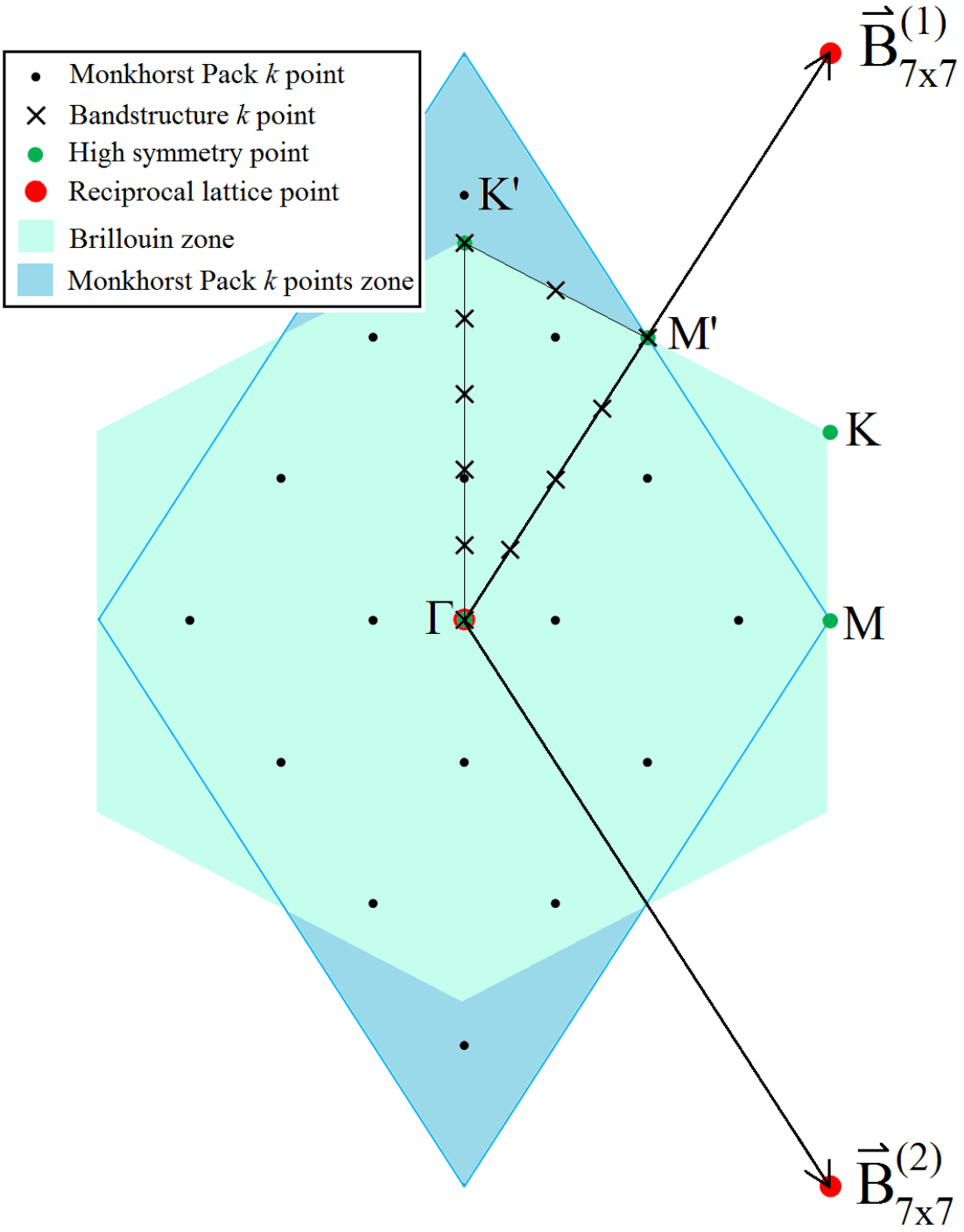

Fig. S.7. *Monkhorst Pack k-points grid used for the main EELS calculations, k-points used for the bandstructure calculations, reciprocal space lattice points, high symmetry points, Brillouin zone and Monkhorst Pack zone.*

Defining the direct-space lattice vectors of the 7 × 7 supercell as

$$\vec{A}^{(1)}_{7\times7} = 7\left(\frac{a}{2}\right)(\sqrt{3}, 1) \text{ and } \vec{A}^{(2)}_{7\times7} = 7\left(\frac{a}{2}\right)(\sqrt{3}, -1)$$

with the graphene unit cell lattice parameter a = 2.46381Å^{-1} (PBE+TS functional), the corresponding reciprocal-space lattice vectors are

$\vec{B}_{7\times7}^{(1)} = \frac{1}{7a\sqrt{3}}(1,\sqrt{3})$ and $\vec{B}_{7\times7}^{(2)} = \frac{1}{7a\sqrt{3}}(1,-\sqrt{3})$.

Using the high symmetry points $\vec{M}'_{(7\times7)} = \frac{1}{2}\vec{B}_{7\times7}^{(1)}$ and $\vec{K}'_{(7\times7)} = \frac{1}{3}(\vec{B}_{7\times7}^{(1)} - \vec{B}_{7\times7}^{(2)})$ which lie within the Monkhorst Pack zone, the *k* point spacings Δk in the bandstructure calculations are:

$\Delta k_{\Gamma\to M'} = \frac{1}{4}|\vec{M}'_{(7\times7)}| = 8.369\times10^{-3}$ Å^{-1} (3 d.p.).

$\Delta k_{M'\to K'} = \frac{1}{2}|\vec{K}'_{(7\times7)} - \vec{M}'_{(7\times7)}| = 9.664\times10^{-3}$ Å^{-1} (3 d.p.).

$\Delta k_{K'\to\Gamma} = \frac{1}{5}|\vec{K}'_{(7\times7)}| = 7.731\times10^{-3}$ Å^{-1} (3 d.p.).

Bandstructures comparison for 6x6 and 7x7 supercells

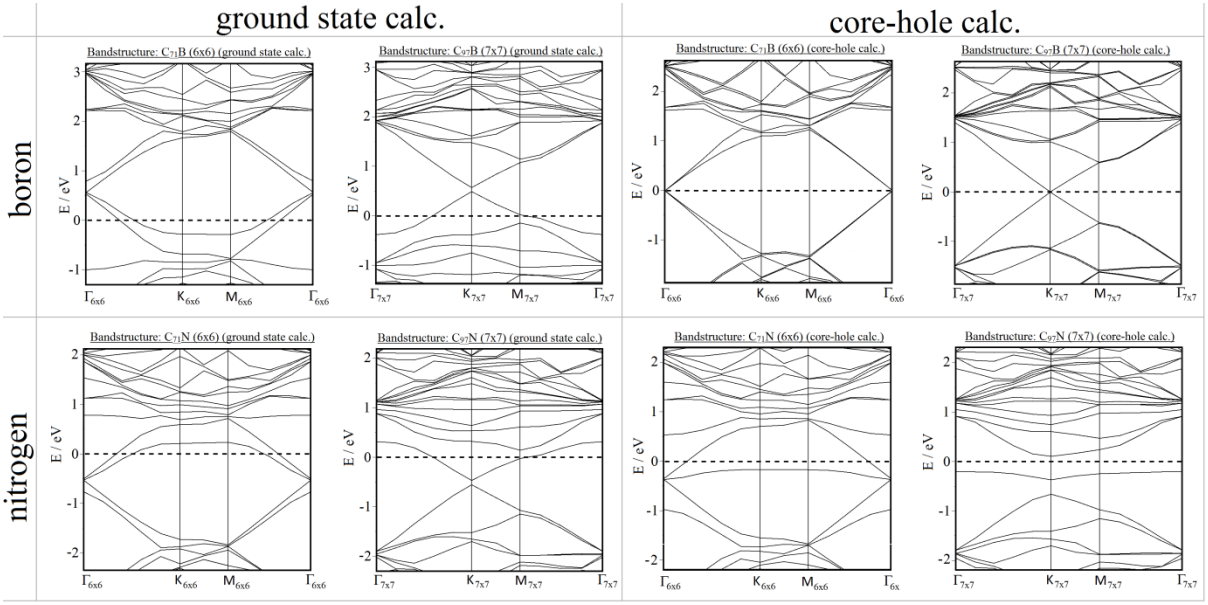

Fig. S.8 *Bandstructures showing the contact or near-contact made by the π and π* bands at the Γ point in 6x6 cells and at the K point in 7x7 cells.*

LDA / PBE+TS functional comparison

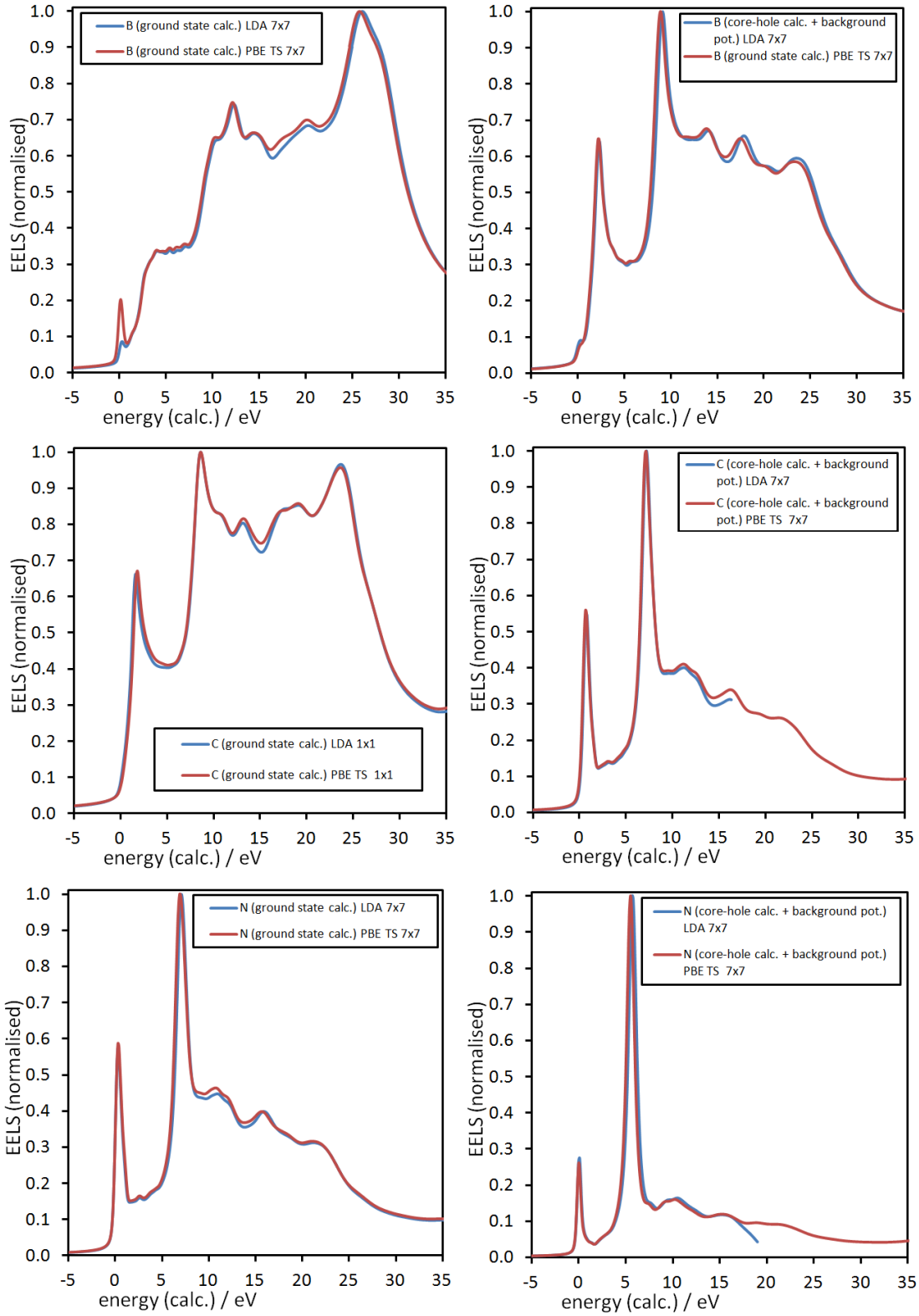

Fig. S. 9 *The insignificant consequences of having to pick between the LDA and PBE(+TS) functionals as shown by the very similar spectra. One standout feature is the "π" peak straddling the Fermi energy in the B ground state case, which is noticeably less intense with the LDA, although still clearly present.*

Slater transition state (half core-hole) calculations with PBE+TS functional

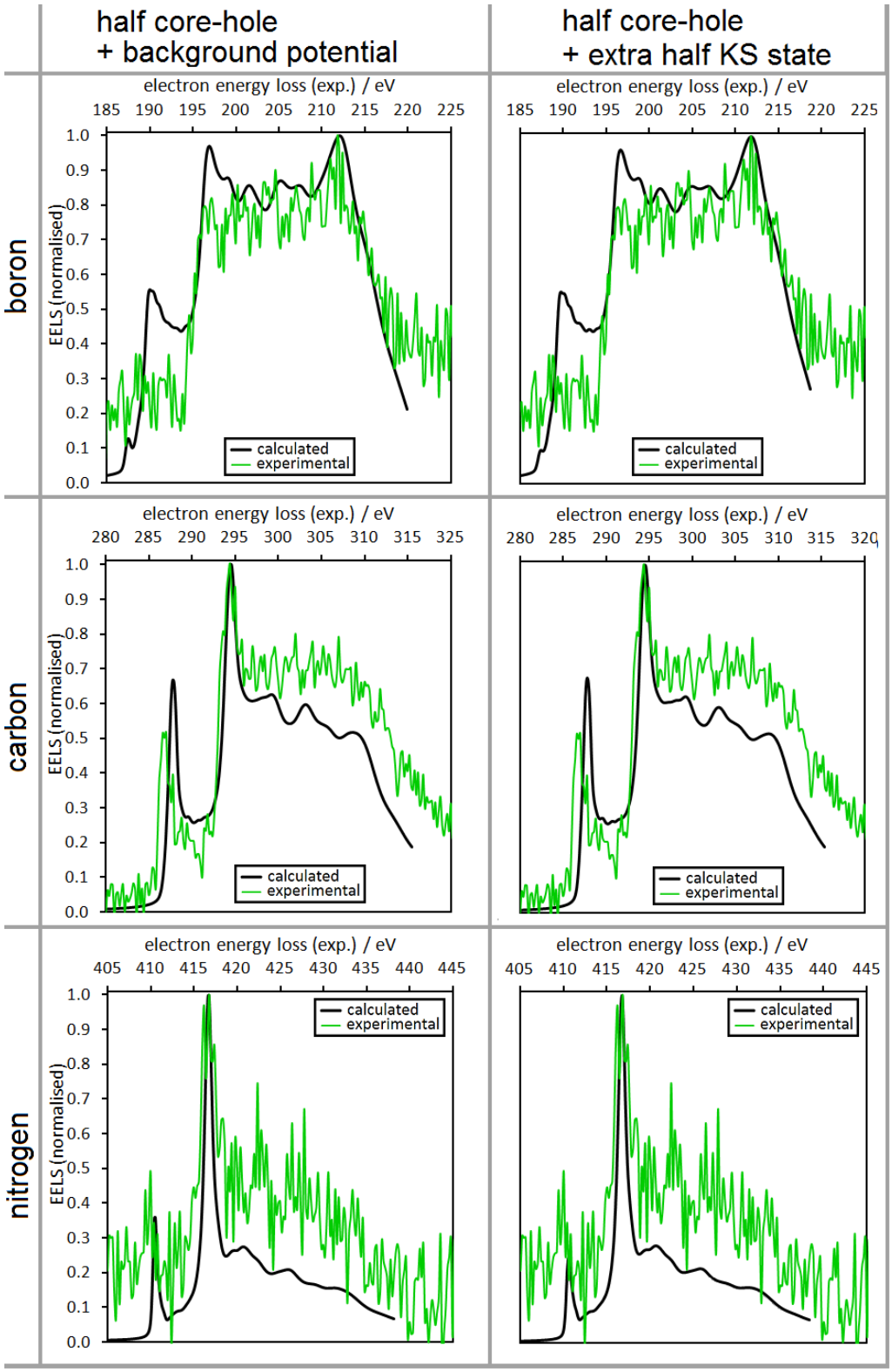

Fig. S. 10 *The comparison of experimental results with half core-holes (Slater transition state) for the B-doped, N-doped and pure graphene cases, using a background potential and half extra Kohn Sham state for neutralisation. These can be compared with the ground-state and full core-hole calculations shown in Figure 1 in the main text.*

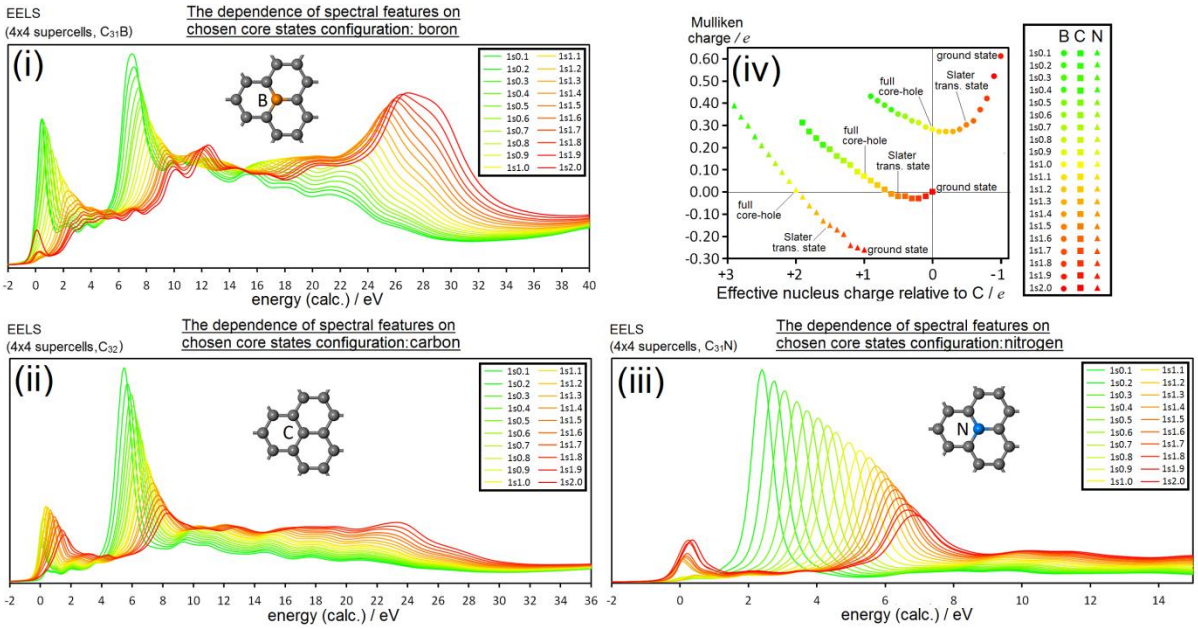

Fig. S. 11 *Calculated spectra using 4x4 supercells with fractional number of core holes from 0.1 to 2.0 in pure and doped graphene. (i) Boron K-edges, (ii) Carbon K-edges and (iii) Nitrogen K-edges. (iv) Mulliken charges vs. effective ionic charge of nucleus with fractional core-hole.*